# Tropical Cyclone Changes in Convection-Permitting Regional Climate Projections: A Study Over the Shanghai Region

**Erasmo Buonomo[1]** [iD], **Nicholas Savage[1]** [iD], **Guangtao Dong[2]** [iD], **Bernd Becker[1]**, **Richard G. Jones[1]** [iD], **Zhan Tian[3]** [iD], **and Laixiang Sun[4,5]** [iD]

[1]Met Office Hadley Centre, Exeter, UK, [2]Shanghai Climate Center, Shanghai Meteorological Service, Shanghai, China, [3]Department of Environmental Science and Engineering, School of Environmental Science and Engineering, Southern University of Science and Technology, Shenzhen, China, [4]Department of Geographical Sciences, University of Maryland, College Park, MD, USA, [5]School of Finance and Management, SOAS University of London, London, UK

**Abstract**   Changes in tropical cyclones due to greenhouse-gas forcing in the Shanghai area have been studied in a double-nesting regional model experiment using the Met Office convection-permitting model HadREM3-RA1T at 4 km resolution and the regional model HadREM3-GA7.05 at 12 km for the intermediate nest. Boundary conditions for the experiment have been constructed from HadGEM2-ES, a General Circulation Model (GCM) from the 5th Coupled Model Intercomparison Project (CMIP5), directly using high-frequency data for the atmosphere (6-hourly) and the ocean (daily), for the historical period (1981–2000) and under the Representative Concentration Pathway 8.5 (2080–2099). These choices identify one of the warmest climate scenarios available from CMIP5. Given the direct use of GCM data for the baseline, large scale conditions relevant for tropical cyclones have been analyzed, demonstrating a realistic representation of environmental conditions off the coast of eastern China. GCM large scale changes show a reduction in wind shear in addition to the expected strong increase in sea-surface temperature. Tropical cyclones from the 4 km historical simulation have a negative bias in intensity, not exceeding Category 4, and a wet bias in the rainfall associated with these cyclones. However, there is a clear improvement in cyclone intensity and rainfall at 4 km in comparison with the 12 km simulation. Climate change responses in the 4 km simulation include an extension of the tropical cyclone season, and strong increases in frequency of the most intense cyclones (approximately by a factor of 10) and associated rainfall. These are consistent with the results from the 12 km simulation.

**Plain Language Summary**   Since global climate models do not have the spatial resolution to simulate tropical cyclones, higher resolution limited area models are commonly used to improve the representation of these phenomena. In this study, where changes in the Shanghai area have been estimated, this was done in two steps, using a regional model at 12 km resolution as the intermediate step to finally reach a 4 km resolution for the region around Shanghai with a model which can explicitly represent convection processes. This was done by using one of the warmest climate scenarios available from the climate projections run under realistic increases of greenhouse-gas concentrations, to study climate change at the end of this century. The global climate model reproduces large scale conditions relevant for tropical cyclones which compare well with observations in the historical period and projects changes in the atmosphere and the ocean which are relevant for tropical cyclones. The downscaled model at 4 km reproduces the observation with some biases in intensity, not sufficient to reach Category 4, and in the cyclone precipitation, through marked improvements with respect to the 12 km model. The climate change response shows a strong increase in intense tropical cyclone frequency and rainfall, common to both models.

## 1. Introduction

Tropical cyclones are a major hazard facing Chinese coastal provinces. From 1951 to 2008, 532 tropical cyclones made landfall in China and during the 1983–2008 period there were 11,502 deaths, with an annual average of 442 deaths due to landfalling tropical cyclones (Fengjin & Ziniu, 2010). Between 1984 and 2015, 249 tropical cyclones caused significant direct national economic losses in China of about 45 billion CNY annually. There was an annual increase of 1.8 billion CNY in losses over this period with the trend mainly due to rapid socioeconomic development (Wang et al., 2016). Wu et al. (2005) analyzed best track data from the Joint Typhoon Warning Center from 1965 to 2003 and found a shift in the tropical cyclone tracks in the western North Pacific, such that

subtropical East Asia has seen an increase in typhoons while the typhoon influence over the South China Sea has considerably decreased. This trend has been confirmed recently by Chen et al. (2022), using data from the Chinese Meteorological Administration (CMA) and the Regional Specialized Meteorological Center Tokyo for the period 1979–2018, which has been shown to be linked to the northward shift of the subtropical high ridge.

With future climate change and economic growth the costs of tropical cyclones are expected to increase worldwide. Mendelsohn et al. (2012) found that the two countries with the largest expected increases in damage due to climate change by 2100 under the SRES A1b scenario would be the United States (USD25 billion $yr^{-1}$) and China (USD15 billion $yr^{-1}$). A damage model coupled with 25 km atmospheric-only GCM driven by prescribed SSTs from coarser resolution coupled simulations (Gettelman et al., 2018) suggests that although the number of storms will decrease by 2081–2100 (Representative Concentration Pathway, RCP, 8.5 and 4.5) strong landfalling storms will increase in East Asia and this will drive an increase in global storm damage by $\sim$50% in 2070 compared to 2015.

While tropical cyclones have a spatial scale of hundreds or even thousands of kilometers, they contain small scale features that are critical to their impacts such as the maximum wind speed and central pressure. Using large eddy simulation, Rotunno et al. (2009) found no convergence in tropical cyclone properties even at resolutions below 100 m and Cécé et al. (2021) found that 30 m seems necessary to produce the vortices which result in the most extreme wind gusts of 132 m s$^{-1}$ over the sea. However, the use of convection-permitting regional climate models (CPMs in the rest of the paper) run at a horizontal resolution of a few kilometers, gives significant improvements in the simulation of tropical cyclones over models with lower resolutions (Knutson et al., 2020; Prein et al., 2015; Taraphdar et al., 2014). Gentry and Lackmann (2010) found that at 4 km resolution the model was able to simulate tropical cyclones features such as polygonal eyewall segments but that a grid spacing of 2 km or less is needed for representation of important physical processes in the tropical cyclone eyewall. For operational prediction, they recommended a grid length of 3 km or less. Therefore, a CPM with a horizontal resolution of 4 km seems likely to provide significant improvements in simulation over a model with parameterized convection at lower resolutions typically used in regional climate models (RCMs) of 10–25 km.

To date most simulations addressing the influence of climate change on tropical cyclones using these CPMs have run with targeted higher resolution only for periods where there are active tropical cyclones in the lower resolution modeling. To determine the impacts of climate change, most of these studies use Pseudo Global Warming approach (Schär et al., 1996), whereby regional climate change simulations are generated by perturbing reanalysis boundary conditions, used as a baseline for the historical climate, with multiannual monthly or seasonal average changes for each variables in the boundary forcing from averaging GCM from model intercomparison projects (e.g., Gutmann et al., 2018) or to a set of single GCMs (e.g., Knutson et al., 2013). The procedure is expected to generate regional projections which capture the main thermodynamics signal due to climate change, while averaging all the effects due to the GCM variability and smoothing the effect of their circulation changes. This may be for a single tropical cyclone case of interest, for example, Thompson et al. (2021), Mittal et al. (2019), Kanada et al. (2017), for larger number of tropical cyclones (Gutmann et al., 2018; Kanade et al., 2013; Kanada et al., 2020 from 4°C simulations in Mizuta et al., 2017), of for specific basins (Knutson et al., 2013, 2022, North Atlantic, Wu et al., 2014, North West Pacific). These studies have shown robust results in projecting increased maximum lifetime intensity under climate change and precipitation, increased depth of tropical storm structures. Changes in frequency estimated from basin-wide studies from convection permitting models seem to be project more robust changes (with changing driving conditions) with respect to their coarser resolution driving models (Camargo, 2013; Tory et al., 2013).

In contrast, the modeling approach used in this study is based on the direct use of high frequency boundary forcing from single GCMs, following the experimental protocol from the CORDEX project (Giorgi et al., 2009). This approach can be justified from the need to generate high impact climate scenarios, for which climate change cannot be assumed as a perturbation of the present climate and it has already been applied in a previous study over the Western North Pacific region (Gallo et al., 2019) showing a plausible representation of tropical storms in the area and climate projections consistent with the present literature (e.g., Knutson et al., 2020). In order to generate a high impact scenario for the Shanghai region (Figure 1, left) for multiple flood hazards, with a focus changes to tropical cyclones, two 20-year runs downscaling HadGEM2-ES (Collins et al., 2011) for the Western North Pacific region have been carried out. The simulations use two nests, the outer covering the whole region at 12 km resolution and the inner covering the region around Shanghai at 4.4 km resolution (Figure 1, right). The
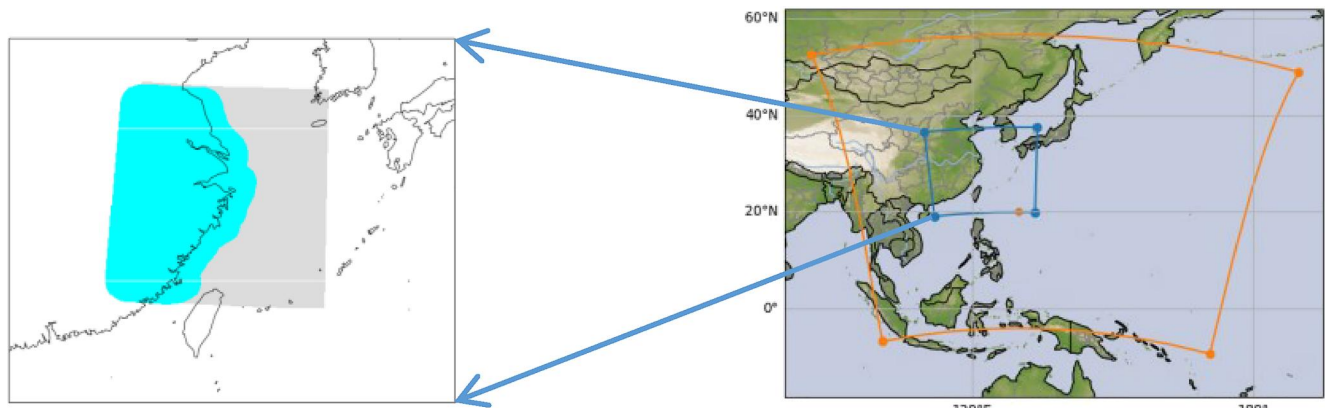
**Figure 1.** Schematic of the Shanghai cyclone warning area (117°–127°E, 26°–34°N), with the analysis region including the coastal area near Shanghai in blue (left panel) and outline of the 12 km domain (orange) and the 4 km domain (blue).

simulations have been run for the historical period of 1981–2000 and for the future period of 2079–2099 assuming the RCP8.5 emissions scenario. Section 2 describes the experimental design, including model set up, and observational data sets used for the evaluation. Section 3 provides an assessment of GCM large scale features relevant for tropical storm in this region and on the skill of the limited area models in reproducing them. It is then followed in Section 4 by a detailed evaluation of tropical cyclones simulated at 12 and 4 km, based on a number of metrics directly comparable with observation in order to assess the skill of the two limited area models, and an estimate their changes from this projection. All the findings are then discussed in the concluding section.

## 2. Experimental Design, Model Description and Evaluation

The 4 km resolution simulations were carried out by using a state-of-the-art CPM from the Met Office, an outer nest at 12 × 12 km resolution, driven by lateral boundary conditions and Sea-Surface Temperature (SST) and sea ice data from HadGEM2-ES simulations and an inner nest at a resolution of 4 × 4 km resolution driven by the 12 km outer nest. This section provides details of the driving GCM used and the configuration of the two LAM nests. Twenty-year baseline and future climate simulations of the nested models were run using these boundary conditions and atmospheric greenhouse-gas and aerosol concentrations from the corresponding periods in the HadGEM2-ES simulations. The baseline simulations were run for 1981–2000 under historical emissions and the future climate simulations for 2080–2099, driven by emissions from the RCP8.5 scenario (van Vuuren et al., 2011). These choices correspond to some of the most extreme climate change conditions available from projections from the fifth phase of the Coupled Model Intercomparison Project (CMIP5, Taylor et al., 2012), by taking the end period of the very high emission concentration pathway for a GCM with a high climate sensitivity, with a global temperature change of ∼4.8°C between the two periods downscaled in this study.

### 2.1. Boundary Conditions From Driving Global Model

Lateral boundary conditions for the outer nest come from 6 hourly data from HadGEM2-ES (Collins et al., 2011) and uses the simulations from the CMIP5 historical and RCP8.5 experiments (described in Jones et al., 2011). Daily SST and sea ice data in both the outer and inner nests are also derived from these simulations. The GCM was run at a horizontal resolution of 1.25° × 1.875° in latitude and longitude with 38 model levels to a maximum height of over 39 km for its atmospheric component and its ocean model was run at a zonal resolution of 1° everywhere and a meridional resolution of 1° between the poles and 30° latitude, then increasing smoothly to 1/3° at the equator.

### 2.2. Nested Model Domains

The outer and inner nests are shown in Figure 1 (right panel). The outer nest was chosen to cover the major cyclogenesis region for tropical cyclones that impact Shanghai, based on tracks from Chinese Meteorological Agency included in the International Best-Track Archive for Climate Stewardship (IBTrACS, Knapp, Kruk,

et al., 2010). These domains also allow enough time and space for the models to spin up to its true resolution over the regions of interest. If too small a domain is chosen, then the model will show little increase in effective resolution over the driving model (Jones et al., 1995; Leduc & Laprise, 2009), while a larger domain may lose the large scale consistency with the driving model (Jones et al., 1995) or could be too expensive computationally. The 12 km domain used in this study has been based on the domain used by Gallo et al. (2019) for a study on the NW Pacific region, which also used HadGEM2-ES to drive a previous version of the 12 km model of this study, and on the domains used for two downscaling experiments over China (Amato et al., 2019; Jiang et al., 2020), since these 12 km simulations are also expected to generate useful data for this country. The 4 km model has been chosen after sensitivity tests using the present double-nesting modeling setup, based on a series 1 year runs using ERA-Interim reanalysis (Dee et al., 2011). Both models have a rotated pole located at 310°E, 70°N giving a quasi-uniform grid spacing over the whole domain.

### 2.3. 12 km Regional Climate Model

The 12 km RCM (HadREM3-GA7.05, Tucker et al., 2022) is a limited area configuration of the GA7.05 model (Walters et al., 2019), closely based on the 12 km model configuration used in UKCP18 climate projection (Murphy et al., 2019; Tucker et al., 2022) with some further modifications described here.

The RCM has a grid with $0.11° \times 0.11°$ resolution and a 4 min timestep and has 63 levels (with an upper lid at ~39 km). The model top used in this experiment is slightly lower than that used in the configuration of Tucker et al. (2022), to allow all 63 levels to sit below the HadGEM2-ES model lid. It is driven at its lateral boundaries in a one-way nesting approach, using time series of surface pressure, wind, temperature and moisture values archived every 6 hr from HadGEM2-ES, and applied to the RCM across a 10-point relaxation zone (Davies, 2014). Inside this, orographic heights on the global and regional model grids are blended across a further three points. The RCM therefore adjusts to the surface and lateral boundary forcing across a 13-point external rim. Both RCMs simulations evolve freely in their internal domains and respond to surface orography specified at their native grid scale. No nudging or parameter perturbations were used in either model configuration.

Convection is parameterized using a mass-flux approach based on Gregory and Rowntree (1990), large scale microphysics is a single-moment scheme derived from that of Wilson et al. (1999) and large-scale cloud is based on the prognostic cloud fraction and prognostic condensate PC2 scheme.

The land surface model used is the Joint UK Land Environment Simulator (JULES, Best et al., 2011; Clark et al., 2011) with the surface of each land grid box subdivided into five types of vegetation (broadleaf trees, needle-leaved trees, temperate C3 grass, tropical C4 grass and shrubs) and four non-vegetated surface types (urban areas, inland water, bare soil and land ice). There is no urban land use change over time however the disturbed fraction of the natural vegetation changes is based on the CMIP5 scenarios (Hurtt et al., 2011).

It was decided not to include the GLOMAP-mode aerosol scheme as an interactive component of the RCMs, primarily due the computational expense of this scheme. Instead aerosol radiation and cloud effects are derived from the MACv2-SP data set for the historical (Stevens et al., 2017) and RCP8.5 scenarios (Fiedler et al., 2019) The method used to implement these scenarios is identical to that used in the 12 km RCM in UKCP18 (although with a different source data set). Monthly 3D fields of shortwave and longwave optical properties (absorption, extinction, scattering and asymmetry) and cloud droplet number concentration on the 12 km model grid were calculated and then these were prescribed as a time series in the RCM simulation for use in its calculation of time-varying radiative forcing. The same approach for aerosol was used in the 4 km model.

### 2.4. 4 km Convection-Permitting Model

The model used for the inner nest (HadREM3-RA1M) is the CPM derived from the RA1M configuration (Bush et al., 2019) as used in the UKCP18 climate projections (Fosser et al., 2020). As the key region of interest is in the sub-tropics, it was not clear whether a tropical or mid-latitude configuration was more appropriate and it was decided to proceed based on the mid-latitude configuration apart from the vertical level set (see below).

The CPM has a grid with $0.0405° \times 0.0405°$ resolution and a 100 s timestep. Also due to the low top of the 12 km model used here, the RA1T vertical levels were used, consisting of 80 model levels and a model top at 38.5 km. It is one-way nested within the 12 km model using surface pressure, wind, temperature and moisture values archived every 3 hr and has a nine-point relaxation zone (Davies, 2014). Inside this, orographic heights on the global and

regional model grids are blended across a further 33 points. This configuration runs with the convection parametrization switched off (hence "convection-permitting"), relying on the model dynamics to explicitly represent convection. The cloud microphysics used is a single moment scheme based on Wilson et al. (1999), with modifications as outlined in Bush et al. (2019). Liquid cloud amount is parameterized with the diagnostic Smith (1990) scheme with ice cloud fraction diagnosed from the ice water content.

The same land surface model (JULES) is used as in the outer nest. Due to a lack of suitable urban morphology data sets for the region of interest, no urban roof tile has been used (unlike in the UKCP 2.2 km resolution runs but consistent with the outer model nest in these experiments).

### 2.5. Tropical Cyclone Tracking Methodology

Three-hourly fields of mean sea level pressure (MSLP), 400 hPa temperature and 10 m windspeed were used for tracking tropical cyclones using the TempestExtremes software (Ullrich & Zarzycki, 2017). The tracking algorithm has two parts—the initial feature detection and then the stitching of these features to generate realistic tracks.

The feature detection was based on finding minima in air pressure at sea level with features within a radius of 6° of each other being merged. A feature is then further refined with two "closed contour" criteria. First it must have an increase in MSLP of at least 200 Pa (2 hPa) within 5.5° of the candidate node (pressure minimum condition). Second there must be a decrease of 0.4 K in 400 hPa air temperature within 8°of the node using the maximum temperature within 1.1° of the candidate as a reference temperature (warm core condition).

The stitching part used a maximum distance between features of 3°, a minimum track length of 16 points (48 hr), a minimum path distance of 8° and allowed a 3-hr gap between successive track points. A topographic filter, a filter on maximum windspeed and a latitude filter have been applied. The topographic filter applied checked the altitude of the earth's surface at the location of the nodes–tracks were rejected if they did not have at least 48 hr at with a surface altitude less than 100 m and at least 24 hr at a surface altitude less than 10 m. The filter on windspeed rejected points if they did not have maximum 10 m windspeed of at least 17 m/s at one timestep. Finally, tracks were also rejected if they did not have at least 20 points (2.5 days) south of 40°N. It was found that some spurious features were detected at the edge of the domain which were not physically realistic but occasionally were included in the stitched tracks leading to unrealistic tracks so after the feature detection all features within 4 grid boxes of the model edge are ignored.

### 2.6. Observations and Reanalyses

A number of observational and reanalysis data sets have been used to evaluate model simulations. The NOAA National Oceanic and Atmospheric Administration Optimum Interpolation SST (NOAA OI SST) v2 (Huang et al., 2021; Reynolds et al., 2007) is a global ¼° resolution data set of SST based on a combination of satellite, buoy and ship observations available from September 1981 to the present day.

The CPC Morphing Technique (CMORPH) High Resolution Global Precipitation Estimates, Version 1 (Joyce et al., 2004; Xie et al., 2019) is a global (60S–60 N) data set of bias-adjusted satellite precipitation observations at a spatial resolution of 8 km × 8 km (at the equator) and with a temporal resolution of 30 min. The data are available from 1 January 1998 to the present, which is outside the historical period used in the downscaling experiment: the earliest 21-year period, 1998–2018, has been used for model evaluation.

ERA-Interim (Dee et al., 2011) is a global atmospheric reanalysis, available from 1 January 1979 to 31 August 2019. The horizontal resolution is ∼80 km, daily and monthly averages have been derived from the 6 hourly instantaneous atmospheric variables used in this study.

CN05.1 (Wu & Gao, 2013) is a gridded daily data set over China of daily mean, minimum and maximum temperature and precipitation for the period 1961–2005, at a resolution of 0.25° × 0.25°. The data set is based on interpolation of observation anomalies from over 2400 observing stations in China.

The IBTrACS data of tropical cyclone tracks are used to provide composite footprints of precipitation for the tropical cyclone evaluation. As described in Knapp, Kruk, et al. (2010) this data set is a centralized repository of global tropical cyclone best-track data from the RSMCs and other agencies. Tracks from CMA, which is responsible for monitoring tropical cyclone activities the region of interest considered here, have been used in this work.

## 3. GCM Environmental Conditions in the Present and Future Climate

The use of high frequency boundary data from the GCM ensures the physical consistency between SST and atmospheric forcing from synoptic time scales to lower frequency variability for both the historical and the future climate period. This is particularly important for the simulation of a worst-case scenario, for which the methodologies based on perturbing boundary conditions from reanalysis with monthly or lower frequency changes might not be able to capture all relevant changes in the atmospheric structure. However, the choice of using high frequency GCM output as boundary conditions for this experiment requires an assessment of the relevant large-scale processes reproduced by the historical simulation, following the same principles used in designing downscaling experiments from CMIP5 GCMs (e.g., McSweeney et al., 2015).

Since the main purpose of this work is to generate climate change scenarios of tropical storms, this section assesses variables with a direct impact on tropical storm formation and development (e.g., Gray, 1998). The analysis includes SST, prescribed to the corresponding daily variable from the driving GCM, and large -scale atmospheric variables likely to be well represented at GCM scales in both stages of the double nesting experiment. A key criterion of RCM simulations is that the large scale meteorology resolved by regional model should be consistent with that of the driving model (Jones et al., 1995). The expected consistency of these variables at GCM scales from the limited area models is also discussed. Other variables such as relative vorticity and humidity variables are not compared, since they are mostly likely to be determined by the scales well resolved at the RCM resolution in this experimental setup with a free evolving atmosphere in the interior of the two nested domains.

### 3.1. Sea Surface Temperature

The historical period from HadGEM2-ES has been compared to the NOAA OI SST v2 data set in Figure 2. The temperature gradients in the Western North Pacific are captured well by HadGEM2-ES and the biases are typically ±1 K with larger biases ranging between ±2.5°C, negative between Japan and the continental coast and in the open ocean, positive in northernmost parts of the domain. For the purpose of this study, the small bias over the South China sea supports the direct use of this variable as a background to generate a realistic climatology of tropical storms for the region of interest in this study (Figure 1). This is a feature which is also present in autumn (Figure S1 in Supporting Information S1), where the largest negative bias is in the northern part of the North Pacific gyre while the negative bias in the northern coast changes sign around 45°N, and it also extends to the standard deviation of seasonal means in both seasons (Figure S2 in Supporting Information S1), both with positive bias over the northern part of the domain and a negative bias along the coast, reaching the South China sea in autumn. In both seasons, there is a good representation of the region with $T > 26°C$, usually indicated as the threshold for formation of tropical storms (Gray, 1998), in particular in its northward reach near the coast.

This figure also shows the pattern of the climate change response for the future period simulated (2080–2099). There is an increase of ~3.5°C over the tropical region and including the area of interest, while larger temperature increases of up to ~7°C are shown in the north of the domain, with a southern extension over the coastal areas of Japan, Korea, and northern China. It is not clear how this change will affect tropical storm frequencies in the future climate, since increased SST thresholds in a warmer world have been hypothesized (e.g., Emanuel & Nolan, 2004) and shown in idealized experiments (e.g., Sugi et al., 2015), with a number of physical processes involved in the process (e.g., summary in Sobel et al., 2021). However, SST is related to tropical storm intensity (e.g., Miller, 1958; Emanuel, 1987 for the theoretical links with maximum potential intensity, Xu and Wang (2018) for the link with the intensification rate in the West Pacific), which is expected to increase under climate change. A similar pattern of changes has been found in autumn (Figure S1 in Supporting Information S1), which increases the colder baseline temperature above the 26°C threshold. For the given future period and concentration pathway, this change generates SST patterns reaching the same extent as in summer in the historical climate.

### 3.2. Atmospheric Boundary Conditions and RCM Consistency

Wind shear is used in this section both as one of the key environmental variables for tropical cyclone formation and development (Gray, 1998), but in this context it is also discussed in terms of its individual velocity components at different levels since skill and climate change responses are the result of the combination of velocities at different levels.
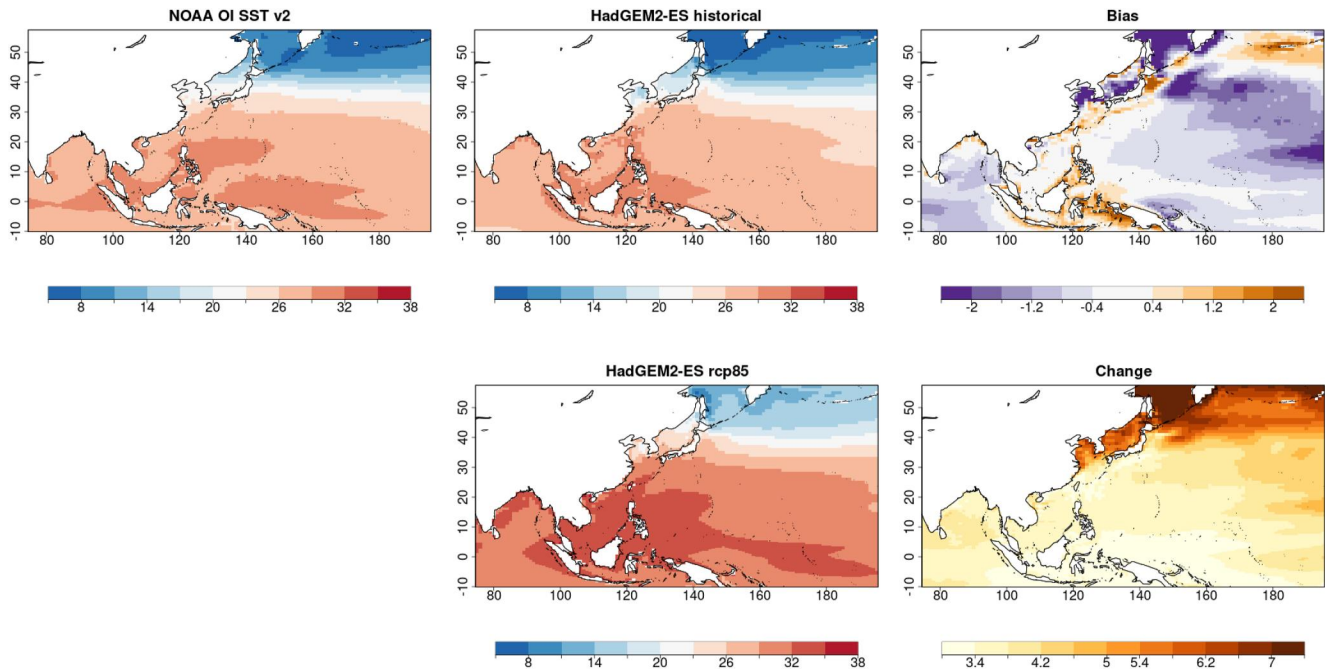
**Figure 2.** Multiannual mean sea-surface temperature (SST), summer (JJA), °C. Top: HadGEM2-ES historical simulation, 1981–2000 (left), NOAA OI SST v2, 1981–2000 (middle), HadGEM2-ES bias (right); bottom: HadGEM2-ES rcp8.5, 2080–2099 (middle), climate change (right).

The specific metric used for this analysis is the Environmental Wind Shear (EVWS), defined as the modulus of the difference between the 250 and the 850 hPa horizontal wind vectors. Previous studies have identified a limit of 10 m/s as the maximum value which favors formation and development of tropical storms (Magee et al., 2016). The top row of Figure 3 compares this metric for the June to August season in ERA-Interim and the historical simulation of HadGEM2-ES. For the historical period, HadGEM2-ES overestimates this parameter south of 20° N, but the cyclogenesis and development region relevant for southern China, mostly north of this latitude, is well represented, including a good comparison with the number of days of favorable conditions for formation and development of tropical storms. The bias is both due to the overestimated eastward flow at 850 hPa over southeast Asia and, to a lesser extent, to the weakness of the tropical easterly jet over this region, an issue which still affects CMIP6 GCMs (Huang et al., 2020). The comparison with horizontal winds from reanalysis at 850 hPa and 250 hPa is included in the Supporting Information S1 (Figure S3). The bottom row of Figure 3 shows the climate change response for this parameter for the June to August season. There is a strong reduction of EVWS associated with the monsoonal flow in southern Asia at 850 hPa, a robust feature of climate projections (Wang et al., 2021), with a smaller decrease over most of the West Pacific in the Northern Hemisphere, the latter related to the southward shift of the upper troposphere sub-tropical jet.

The EVWS from the HadGEM2-ES historical simulation in the autumn months (SON), shown in the Supporting Information S1 (Figure S4), is dominated by a slight southward shift of the dominant subtropical jet (whose intensity is well reproduced by the GCM) with a smaller contribution from a weaker West Pacific subtropical high (WPSH) with weaker 850 hPa winds extending over the Philippine Sea. Despite the better agreement on horizontal wind intensity and pattern with respect to the summer winds, the fraction of weak wind shear days is substantially overestimated over a zonal band around 10N in the Pacific Ocean. However, the transition from weak to strong wind shear over the East China sea is well captured by HadGEM2-ES. The climate change response (Figure S4 in Supporting Information S1) also indicates a reduction mostly related to a weakened WPSH, with a pattern extended to the coast of China, and an associated strong increase of the fraction of days with EVWS < 10 m/s exceeding 20% over the South China sea. This spatial pattern has been linked to the northward extension of tropical cyclone tracks (e.g., Camp et al., 2019; Chen et al., 2022).

The projected reduction of wind shear and the associated increases of number of days below the 10 m/s threshold is expected to favor the formation and development of tropical storms. Indeed, decreased wind shear has been
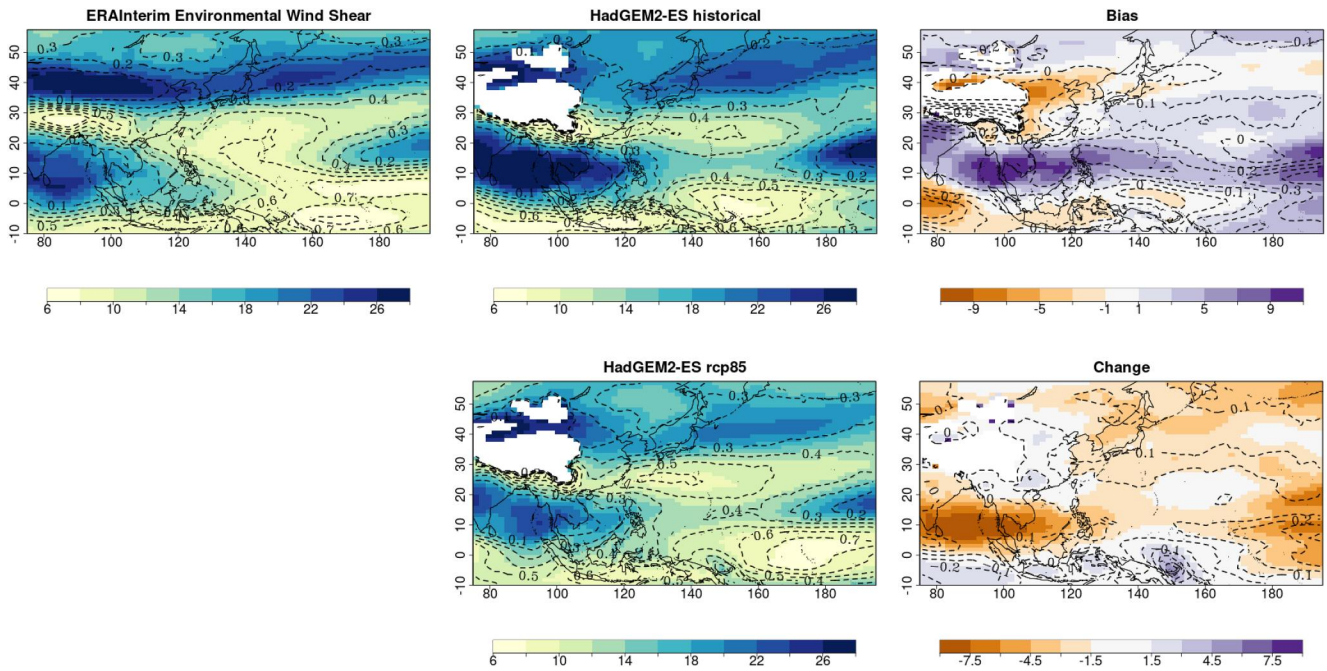
**Figure 3.** Environmental wind shear (EVWS, 250hPa-850 hPa), m/s, multiannual mean, summer (JJA). Top: ERA-Interim, 1981–2000, HadGEM2-ES historical, 1981–2000, HadGEM2-ES bias. Bottom: HadGEM2-ES, RCP8.5, 2080–2099 (middle); climate change response (right). The contour linesindicate the fraction of days with EVWS <10 m/s, in interval of 0.1, condition favorable to tropical storm formation and development.

found to be a contributing factor, in addition to increased SSTs, to a poleward shift of observed tropical cyclones (Kossin et al., 2014).

Figure 4 shows that the realistic environmental conditions imported from HadGEM2-ES are well reproduced in the 12 km RCM simulation, in particular over the main region of tropical storm development for southern China. The main discrepancies can be attributed to the 250 hPa horizontal wind vectors (not shown), including a less intense tropical jet in southeast Asia leading to a decrease in wind shear and a southward shift of the subtropical jet visible as a dipolar pattern in the northern part of the domain in the difference plot. Nevertheless, the magnitude of these differences is relatively small when compared to the average strength of these jets (less than 10% with respect to 20-year mean JJA maximum jet wind speed). Differences of similar magnitudes have also been found
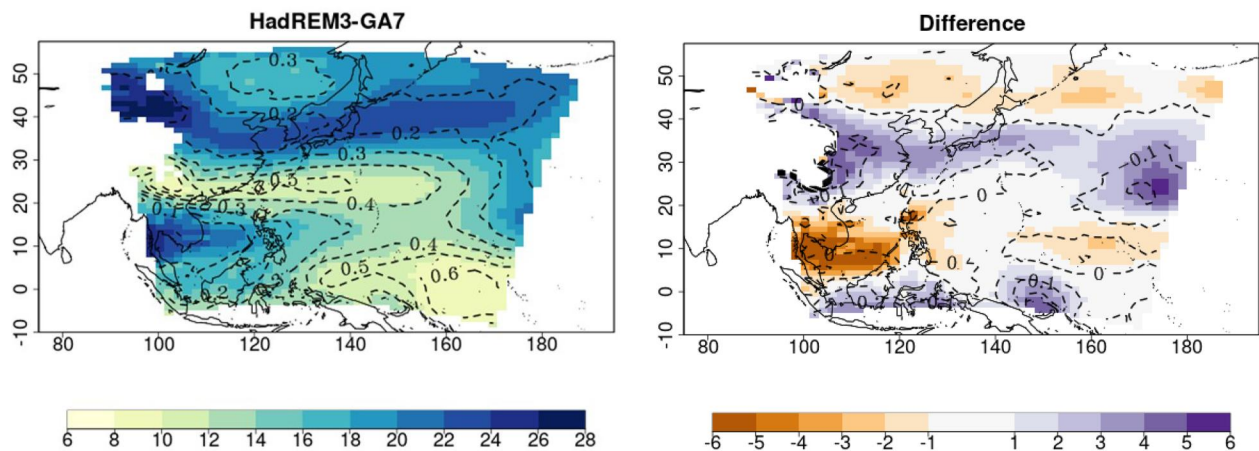


**Figure 4.** Environmental wind shear (EVWS), m/s, summer (JJA), 1981–2000: left: HadREM3-GA7 12 km downscaled by HadGEM2-ES historical; right: Difference between regional climate model and the HadGEM2-ES driving conditions (in Figure 3, top left panel). Contour lines show the fraction of days with EVWS <10 m/s in intervals of 0.1.

for the 20-year mean JJA 850 hPa horizonal wind vector, although in this case the lower wind speed gives a larger relative error ($\sim$20% with respect to the peak mean monsoonal flow). The daily consistency between GCM and RCM winds have been assessed by estimating spatial correlation between the GCM and RCM horizontal winds, after interpolating the RCM wind over the GCM grid. These daily estimates are based on complex vector correlation (Hanson et al., 1992) derived from a generalization of linear regression in complex space, with eastward and northward component representing the real and imaginary part. This results in a complex correlation with magnitude (modulus) linked to the spatial correlation of wind speed and phase linked to the angle between the two horizontal winds over the common domain. In this analysis, the angle is very closely distributed around zero, with a spread (interquartile range) of few degrees, while the magnitude gives a median around 0.6 for the 850 hPa wind, increasing to 0.7 for the 250 hPa wind, and a spread around 0.1. The consistency between the RCM with its driving GCM improved in autumn (Figure S6 in Supporting Information S1), with smaller differences in the EVWS mostly due to small shift in the subtropical jet, a better daily consistency for the horizontal winds at both levels (median of the correlation magnitude around 0.7 for the 850 hPa wind and 0.9 for the 250 hPa wind, with similar spread).

Another factor influencing tropical storm formation is vertical stability (Gray, 1998) which, in this context, has been analyzed from temperature on the same vertical levels used for wind shear (850 and 250 hPa, the latter also for Potential Intensity estimates, e.g. Emanuel, 1987 but also used for tropical storm formation, Emanuel & Nolan, 2004). The comparison of HadGEM2-ES temperatures with ERA-Interim reanalysis (not shown) indicates a very good agreement over the North West Pacific at low level (biases <0.5°C in JJA, cold bias <1°C in SON) and a cold bias over the same region at 250 hPa (<2°C over the tropical ocean in a smooth pattern, similar magnitude in SON with a more complex spatial structure). RCM temperature at the lowest level is very consistent with that of the driving GCM, with a very small difference and a very high day-to-day correlation, while for the upper level, the RCM introduces a warming with respect to the temperature of its driving model which partially correct the HadGEM2-ES bias. The temperature change for HadGEM2-ES under RCP8.5 (not shown) gives smooth patterns of increase of about 9°C over the tropical area under investigation: considering the projected SST increase of $\sim$3.5°C (Figure 2), the estimate upper level amplification is well above the expected doubling of the temperature change at the surface (e.g., Done et al., 2022, but also Knutson & Tuleya, 2004, for $CO_2$ -only forcing). This change in vertical structure is expected to stabilize the atmosphere and counteract the effects of the increased SST temperature on the formation and intensity of tropical storms (Tuleya et al., 2016).

These results confirm a very good degree of consistency between the HadREM3-GA7 and its HadGEM2-ES driving conditions at a time scale which might be challenging for RCMs (Sanchez-Gomez et al., 2009). This outcome, and the realistic description of environmental conditions for tropical storm formation in the HadGEM2-ES historical simulation, should be sufficient to generate a realistic representation of the spatial distribution of tropical storms in the West Pacific area. The analysis of the 12 km downscaled HadREM3-GA7 storms, tracked as described in Section 2.5, seems to support this assumption, showing a good representation of cyclone density (Figure S10 in Supporting Information S1) in particular over the South China sea, while there is a negative bias to the east of the Philippines. A similar pattern of biases have been found for the distribution of genesis locations (Figure S11 in Supporting Information S1). These results can be directly compared with the analysis of Gallo et al. (2019), including a previous version of the Met Office RCM (HadGEM3-RA, Moufouma-Okia & Jones, 2015) also driven by HadGEM2-ES. There are similar biases to the east of the Philippines in Gallo et al. (2019), but the RCM used here shows marked improvement in track density in the South China sea and in the spatial representation of genesis location. Future projections of track densities (Figure S10 in Supporting Information S1) show a northward expansion of track near the coast of China, a feature which has been found in other studies (e.g., Kossin et al., 2016; Tsou et al., 2016), and a very small, non-significant reduction of frequencies ($-$2.2%) over the whole North West Pacific basin, an estimate which is in the upper quartile of frequency changes estimated by Knutson et al. (2020) for this basin for a 2°C global warming.

The analysis in this section is important not only for the validity of the experimental setup of the 12 km simulation, but also as an assessment of the boundary conditions for the convection-permitting model. Since the 12 km outer nest has not degraded the GCM environmental conditions, the CPM is expected to be driven by a good quality downscaled representation of these conditions at 12 km. The inner nest is too small to allow significant divergence from the outer nest, however these variables have been found to be consistent for this domain also (e.g., the vector correlation analysis estimates median magnitudes exceeding 0.9 in all seasons, with mean differences also less than 10%).

### 3.3. Basic Climatology and Climate Change Response From Downscaled Projection

In this section, the results of the comparison of temperature and precipitation from the historical simulations with observations (CN05 gridded data set over land and CMORPH for precipitation over land and sea) and their climate change response are discussed. The main focus is on multiannual means for JJA and SON, the two seasons with tropical cyclone activity. For temperature, the comparison of the CN05 observations with the global model (Figure S7 in Supporting Information S1) shows a warm bias in central and northern China and cold bias over southern China in summer; colder biases become dominant in autumn. The cold bias in both seasons is much reduced by the two limited area models.

The mean precipitation in the historical period for the two seasons examined in this analysis (Figure S8 in Supporting Information S1) has its main bias over the sea, possibly related to a shift toward the northeast of the WPSH in HadGEM2-ES. This bias is subsequently shifted in the same direction in the HadREM3-GA7 projection (see 850 hPa horizontal wind in the Figure S5 in Supporting Information S1) although differences in the parametrization of physical processes between these models cannot be ruled out as the cause, in particular of the positive bias over the South China Sea. In summer, the extension of the low-level monsoonal flow could also be an additional contribution to the positive bias. Over land all the models show a wet bias in southern China and dry bias over the central and northern regions, also supported by a similar behavior from the comparison with the station based CN5.01 data set. The pattern is common to all models and to the two seasons, but stronger for the 4 km CPM and in summer for all models. The main result is that of a bias pattern determined by the driving GCM, but with additional contribution in intensity from the limited area models, the CPM in particular.

The representation of the diurnal cycle of rainfall in tropical regions is a challenge for models relying on parametrized convection, which is not solved by the increase resolution of RCMs (e.g., Nikulin et al., 2012). Despite common biases in precipitation, Figure 5 shows that there are differences in the hour of peak rainfall in the two limited area models. The precipitation over land in the RCM peaks around local noon while the observations (CMORPH) indicate that this peak should be later in the day at about 16:00; in contrast the timing of the peak of precipitation in the CPM is in the mid-afternoon in agreement with observations. The sea is also included in the comparison, this is directly relevant for tropical storms and again the CPM is in much closer agreement on the timing of precipitation than the RCM.

The mean climate change response for surface temperature over land (Figure S9 in Supporting Information S1) also shows that the two limited area models reproduce quite accurately the GCM pattern of changes in the two seasons. The climate change response for precipitation, however, could be affected by local phenomena better resolved at higher resolution. Figure 6 shows the climate change response in precipitation in JJA and SON from the HadGEM2-ES simulation and the two RCM nests. There is a slight increase in summer precipitation over China and reduction over Vietnam. The 12 km RCM shows a strong decrease over the ocean on the east, connected to changes in the position of WPSH (not shown), more pronounced than that projected by the GCM, but it has a very good consistency over the rest of the domain. This consistency is also retained by the more constrained 4 km CPM. In autumn, there is a small increase over China and mainland Southeast Asia and a reduction over the equatorial land area and a zonal pattern of changes over the Intertropical Convergence Zone in the western Pacific, and a reduction off the coast of northern China and Japan, possibly related to the changes in the storm track. For temperature in the same seasons (Figure S9 in Supporting Information S1), the 12 km RCM projected changes are 1–2 K warmer than its driving GCM, in particular over the land areas in the northern part of the domain; over the area covered by the 4 km CPM, instead, the consistency of HadGEM2-ES and the 12 km HadREM3-GA7 responses is quite good, while the 4 km HadREM3-RA1T response is slightly lower. Therefore, as expected, the LAM results are in a good agreement with their driving GCM at regional scale even for surface variables more affected by changes in resolution and physiography.

## 4. Tropical Cyclone Climatology and Climate Change

The skill of the two RCMs in reproducing basic climatological features of tropical storms in the Shanghai region and their changes under greenhouse-gas forced scenarios are presented in this section. The framework for this analysis includes an assessment of metrics which are expected to benefit from the increased resolution in the 4 km CPM, for example, tropical cyclone intensity, but also includes a comparison of tropical cyclone tracks from the 4 km CPM and the 12 km RCM as an evaluation of the consistency between the nested models. Even without initialization over the whole domain, the one-way nesting framework is quite effective in reproducing strong
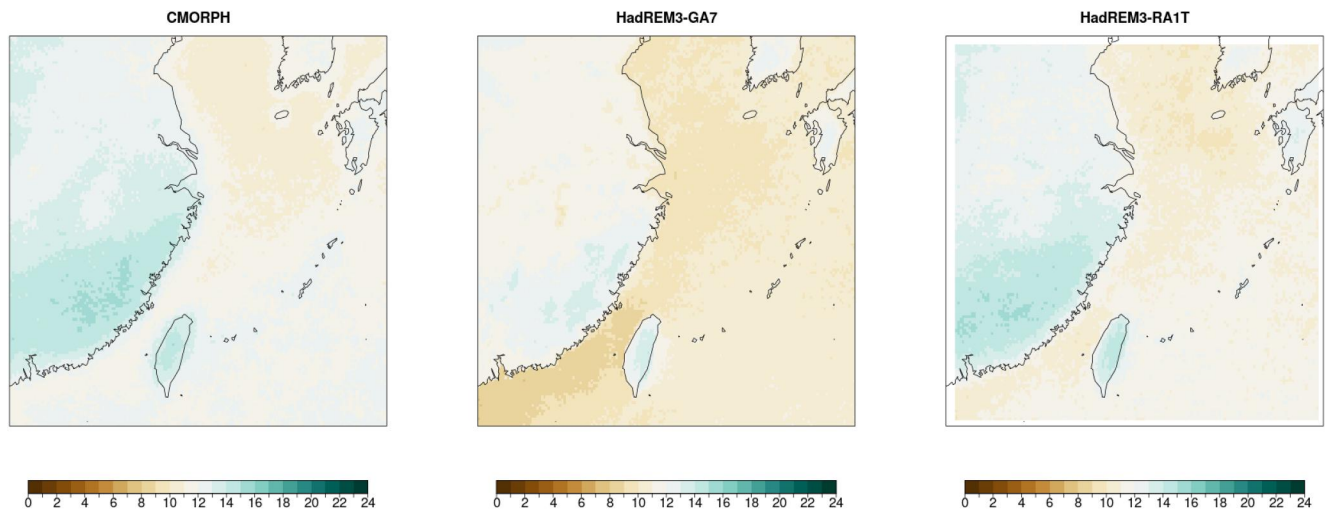
**Figure 5.** Hour of peak daily rainfall (UTC+8) in summer (JJA): left: CMORPH (1998–2018), middle, HadREM3-GA7 12 km historical run, 1981–2000; right, HadREM3-RA1T 4 km historical run driven by HadREM3-GA7.

weather events quite accurately in space and time (Sanchez-Gomez et al., 2009). Therefore, a reasonably high degree of consistency could also be expected in the case of tropical storms. However, the less constrained evolution in the domain interior, which might allow tropical storm formation even in the 4 km domain, and the faster growth of small-scale errors (Lorenz, 1969), which becomes even more apparent when convective events are taking place (Zhang et al., 2003), might lead to a substantially different outcome without invalidating the basic assumptions of the one-way nesting framework. The latter outcome would basically rule out the possibility of reproducing the tropical storm statistics of the 4 km CPM by only downscaling the storms tracked in the 12 km experiment, an approach with clear computational advantages with respect to that used in the present work. The
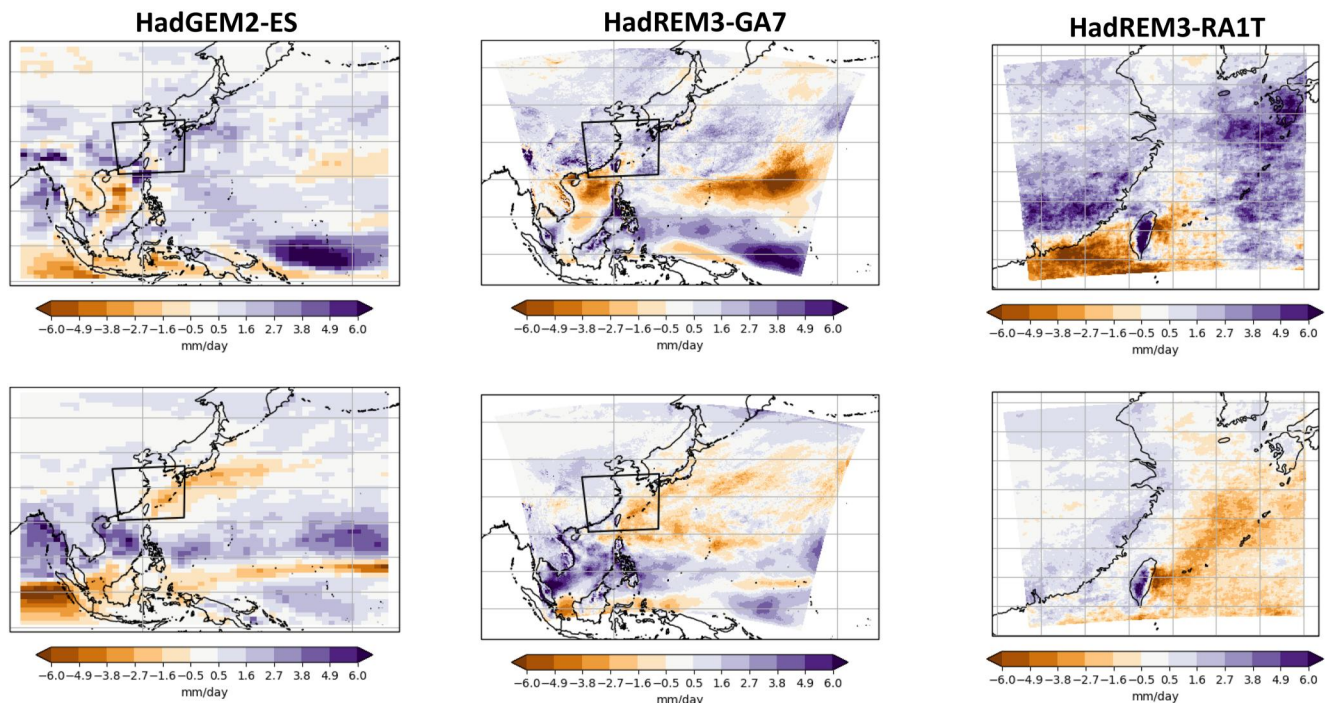


**Figure 6.** Climate change response, precipitation (mm/day), summer (JJA), top row, and autumn (SON), bottom row, estimated as the difference between the historical period 1981–2000 and the RCP8.5 projection for the period 2080–2099 as modeled by HadGEM2-ES (left), 12 km HadREM3-GA7 (middle) and 4 km HadREM3-RA1T (right). The 4 km domain is shown as a black box in the plots of the HadGEM2-ES and the 12 km responses.
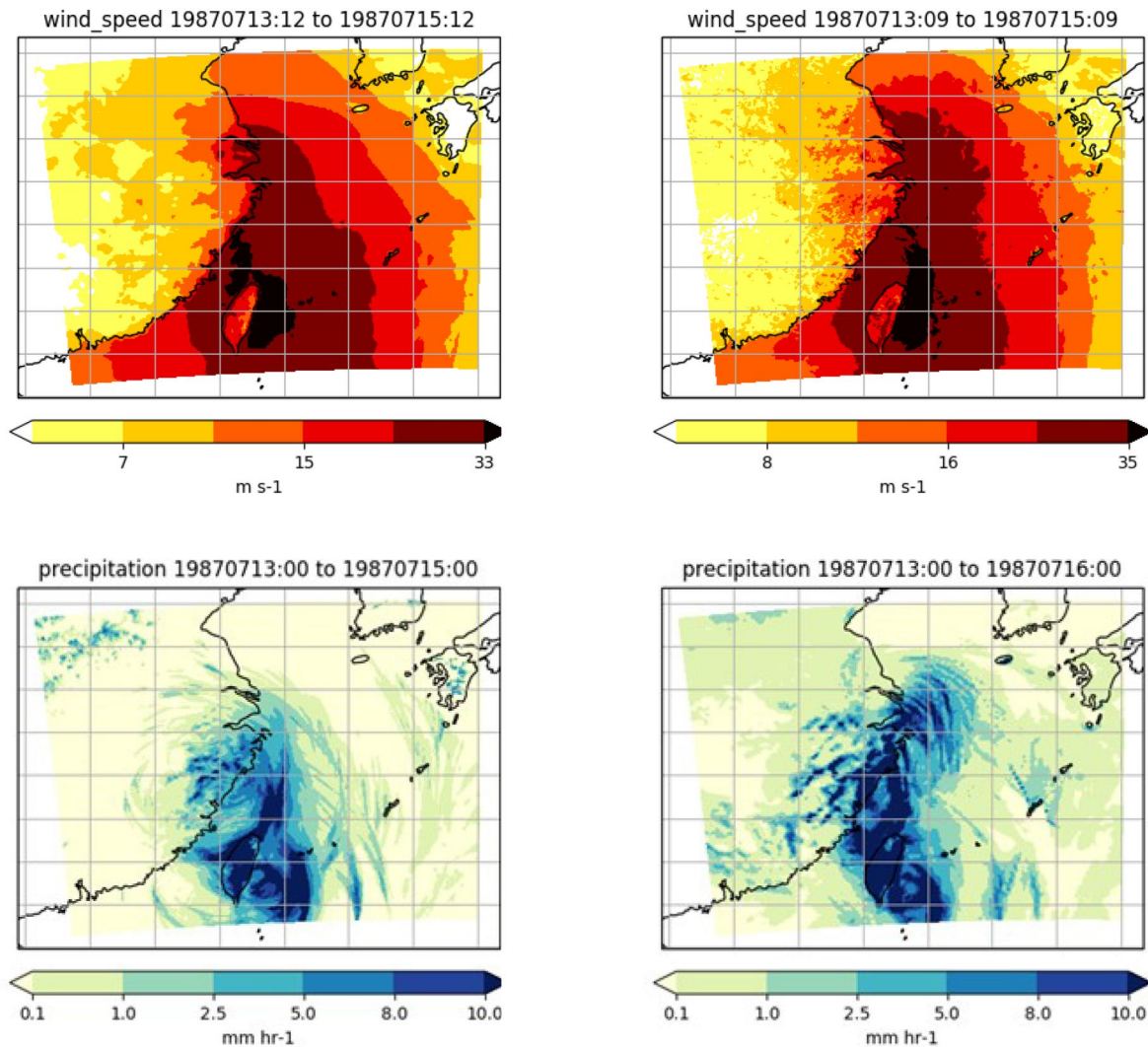
**Figure 7.** Footprints for wind (m/s) and rainfall (mm/hour) for the simulated event detected between 13 and 16 March 1987 in the HadREM3-GA7 12 km simulation (top left: wind; bottom left: rainfall; both fields interpolated on the 4 km HadREM3-RA1T grid), and in the 4 km HadREM3-RA1T simulation.

analysis described in this section is based on 3-hourly tracks from the 12 km RCM and the 4 km CPM simulations which were obtained by using TempestExtremes (Ullrich & Zarzycki, 2017), following the procedure described in the Methodology section.

Some of the effects of the increased resolution can be seen in Figure 7 which shows footprints of a storm from the 12 km RCM historical simulation accurately reproduced by 4 km CPM. For both windspeed and precipitation, footprints are defined as their maximum intensity at each grid-boxes over the whole period of the storm. The resulting fields are quite similar in patterns and intensity distribution, however the 4 km footprints show additional details in the representation of wind and precipitation, in particular at the edge of the storm and over land. This information could be extremely useful in the context of risk modeling, and, in the case of precipitation, difficult to reproduce by empirical models such as those used for wind (e.g., Holland et al., 2010).

The track from the 4 km model used for the footprints in Figure 7 is an example of a storm imported at the boundary region from the corresponding 12 km simulation which compares very well with that from the 12 km driving model. A more comprehensive assessment on such occurrences is based on tracks reaching the coastal region in eastern China defined in Figure 1, with lifetime duration longer than 2 days and maximum wind speeds larger than 17 m/s in the region highlighted in Figure 1. The resulting events are shown in Figure 8. The timing is identified from their maximum wind speed over the area used for tracking in the 4 km simulation, that is, the full
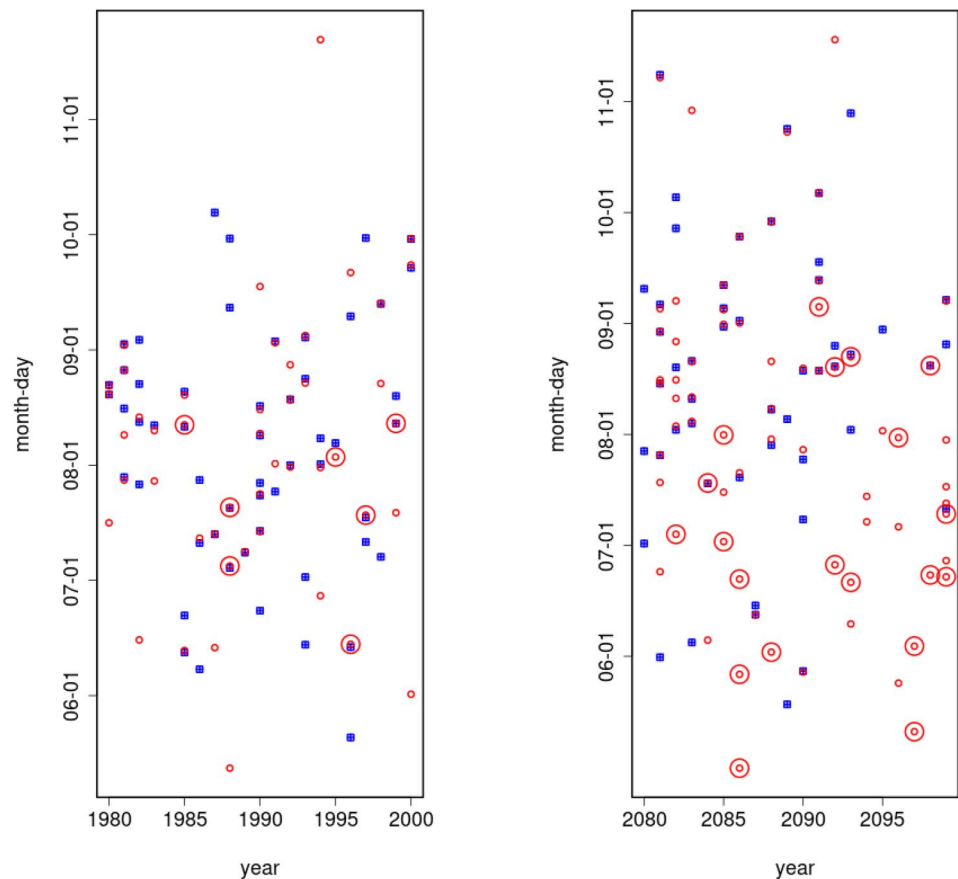
**Figure 8.** Timing of maximum wind speed in the region used to track 4 km storms, for the historical simulations, 1981–2000 (left) and for the RCP8.5 scenario simulations, 2080–2099, for tracks reaching the coastal area in Figure 1 with a wind >17 m/s. In both panels, blue squares indicate 4 km HadREM3-RA1T data, the red circle are for 12 km HadREM3-GA7 data. The larger red circles represent 12 km HadREM3-GA7 trajectories generated within the 4 km tracking region.

4 km domain minus the orographic blending zone and the additional four points removed in the stitching (see Section 2.5). From this metric, matching trajectories in the 12 km RCM and 4 km CPM simulations have been identified as having difference in timing smaller than 2 days. This interval has been taken as a reasonable upper estimate of internal variability in the freely evolving (i.e., not reinitialized) 4 km domain, which is expected to create differences between 4 km trajectories and their corresponding trajectories from the 12 km driving simulations. In fact, the largest number (∼90%) of matching trajectories have their maximum wind speed within a one-day window, also showing a very good match with the rest of the tracks over the area of the 4 km domain. This analysis also shows that there are tracks from the 12 km RCM simulations which have not been replicated in the 4 km model, tracks only present in the 4 km CPM simulations, and a number of coincident or nearly coincident tracks, a small number of which have been generated within the 4 km tracking domain even in the 12 km simulations (i.e., they have not been directly imported from the inner nest boundary zone). The percentage of matching trajectories are 54% and 63% of the total number of tracks for the 4 km RCM historical and RCP8.5 simulations, respectively. This result is confirmed when considering larger areas such as the warning area in Figure 1 with very similar percentages. However, there are more storms detected from the 12 km historical and RCP8.5 simulations with respect to the 4 km runs, with the differences increasing with the size of the analysis area and for the RCP8.5 simulation and significant ($p < 0.1$) for tracks from the 4 km detection area (where numbers of 4 km tracks are 68% and 52% of the number of 12 km tracks for the historical and RCP8.5, respectively). While the latter could be linked to the northward extension of tropical storm tracks in the 12 km simulation discussed in Section 3.2 (which does not seem to be matched by the 4 km simulations), the former could be an indication of problems in reproducing tracks too close to the 4 km boundary region. Statistical analysis (Wilcoxon rank-sum test, Wilcoxon, 1945, as implemented by R core team, 2019) of the dependence of matched and 12 km
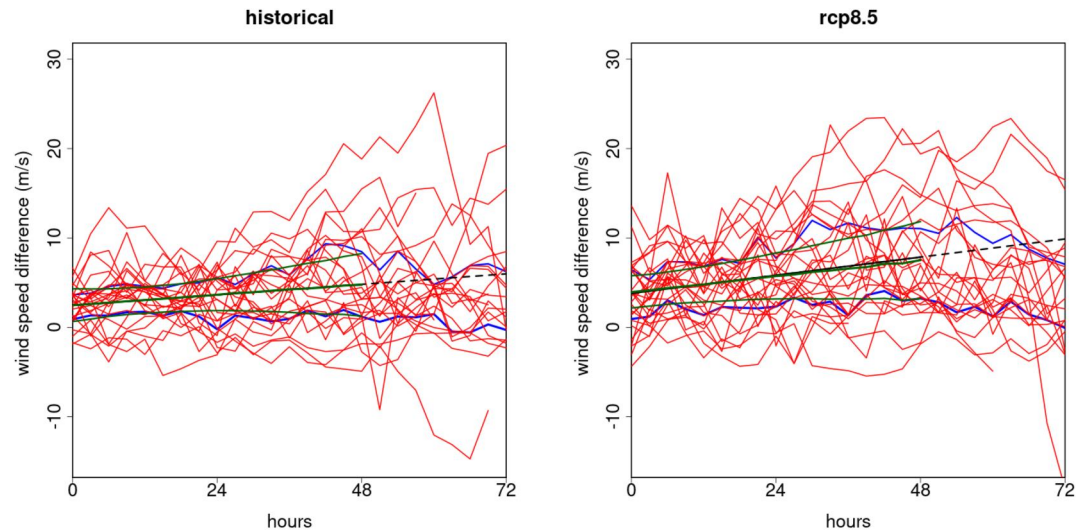
**Figure 9.** Difference in wind speed between matching tracks from the 4 km HadREM3-RA1T model and its driving 12 km HadREM3-GA7 model, as function of time from the entrance in the 4 km tracking domain. Left panel, historical simulation, 1981–2000; right panel, RCP8.5, 2080–2099. Blue lines are estimates of the 25th and the 75th percentiles of differences for each time step. Difference as a function of time have been fit to a mixed linear model with fixed and random effects (Pinheiro & Bates, 2000) both on intercept and in slope, with random effects only dependent on single differences of matching trajectories. For statistical model has been fit in the range [0:48] hours: both regressions give significant estimates ($p < 0.01$) for intercepts (2.5 m/s and 3.9 m/s for historical and RCP8.5 scenarios, respectively) and for slopes (1.2 m/s/day and 1.8 m/s/day for historical and RCP8.5 scenarios, respectively) for the fixed effects. Random effects (slopes and intercepts) are compatible with normal distributions, thereby supporting the use of this statistical model. There is also significant autocorrelation of the residuals from this mixed model, which, however, doesn't drastically change estimates of fixed effects. The black lines are estimated from these estimated fixed effects. These estimates have been done by using the R package nlme (Pinheiro et al., 2021). The green lines are median, 25th and 75th percentiles of predictions from bootstrapped samples (1,000 samples for a number of random tracks equal to those used in the model estimates) which include all random components, using the R package lme4 (Bates et al., 2015). The resulting estimates of these percentiles agree quite well with the estimates from the actual samples of tracks, in particular the model is able to capture the increasing spread with time.

non-matched tracks on their intensity at entry points in the 4 km tracking area has not given significant results; this could be taken as indirect evidence of the strength of the internal variability within the 4 km domain. On the other hand, the non-negligible number of matching trajectories starting within the 4 km domain for which tropical storms are not included in the 12 km boundary conditions (Figure 8) seems to suggest a more limited role for environmental conditions. In the future scenario simulations, there is an 11% increase the number of tropical storms only for the 12 km RCM over the Shanghai warning area, while the 4 km simulations give a small reduction (−5%), with both estimates not significant at 10% level. Over the larger 4 km tracking region, the 12 km simulations give a similar increase (9.5%) but with a smaller p-value (0.07), and a larger reduction from the 4 km simulations (−11%) which is not significant at 10% level. These changes in frequencies, in particular the lack of statistically significant results, are dependent on the choice of a 4 km simulation domain placed at the edge of the tropical storm region (Figure S10 in Supporting Information S1), which is also characterized by spatial variability which might need simulations longer than 20 years to be reasonably sampled at the scale of the 4 km domain. Both limited area models show a lengthening of the storm season with many storms in October, an increased frequency of storms in the autumn months and, to a lesser extent, in early summer with respect to the historical climate (Figure 8).

Another important aspect in nesting the 4 km CPM in the 12 km RCM is the development of features at the 4 km resolution, for which the set of matching tropical storms provide a good test case to monitor their development as they enter the 4 km tracking domain (in analogy with Jones et al., 1995, in which the contribution of mesoscale features from RCMs from the inner edge of the buffer zone has been assessed). Figure 9 shows the differences in maximum wind speed between tracks from matching storms in the 4 km RCM and 12 km CPM in the historical and RCP8.5 simulations. These sets are restricted to the storms generated outside the 4 km domain. For 12 km tracks with multiple entries into the 4 km tracking region, the starting time for 12 km tracks could be easily
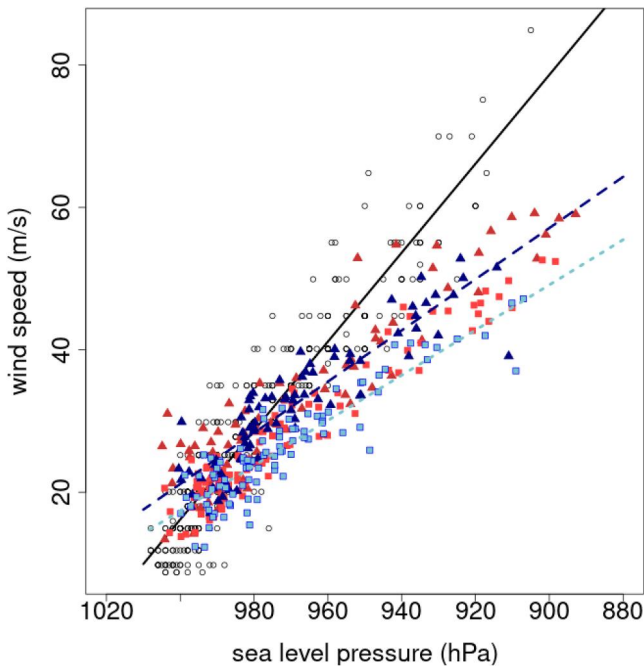
**Figure 10.** Scatter plot of intensity (maximum wind speed within region of analysis) and depth (corresponding minimum sea level pressure) for tracks crossing the eastern China coastal region (see Figure 1) from the Chinese Meteorological Administration (CMA) tracks (black circles), HadREM2-GA7 12 km simulations (squares: blue, all events from the historical period, 1981–2000, red, all events from the RCP8.5 period, 2080–2099), and HadREM3-RA1T (triangles: colors for the same periods as above). Linear fit (black line) estimated from the CMA set of tropical storms, blue dashed line for the 4 km HadREM3-RA1T tracks and dashed cyan line for the 12 km HadREM3-GA7, both estimated from the historical simulations.

identified from the closest time to the start of the corresponding 4 km tracks. The 4 km HadREM3-RA1T tracks show stronger maximum wind speed for at least three quarters of the tracks at all time steps. These differences have been fitted to a mixed linear model (Pinheiro & Bates, 2000), with fixed effects representing intercept and slope common to all the maximum wind speed differences of all matching trajectories. There is evidence of effective spin-up before the entrance of the 4 km tracking region (fixed effect intercept values of 2.5 m/s and 3.7 for historical and RCP8.5, respectively, both with $p < 0.01$), taking place in a region which is ~150 km wide around the analysis region (for comparison purposes, the typical translational speed of tropical storms is around 20 km/hr, Kossin, 2018). This is followed by a slower increase for the following 2 days (fixed effect slopes are 1.2 m/s/day and 1.8 m/s/day for the historical and RCP8.5 simulations, also with $p < 0.01$), after which the interaction with land becomes more important. Even if the intensification in the first 2 days is small in the context of the variations of single tracks, it is an indication that not all the tracks in the 4 km model might have developed their fully resolved features, therefore their maximum intensity over the domain might be underestimated in a way that is difficult to evaluate from this kind of analysis.

Figure 10 is a depth versus intensity plot which uses the same tracks discussed above, a relationship commonly used to visualize effects due to the increased resolution (e.g., Knutson et al., 2015; Roberts et al., 2020). These points have been estimated from the time step with maximum wind speed over the 4 km tracked region from all 4 km CPM and 12 km RCM tracks. Simulated data are not following the steeper straight line estimated from the CMA observed tracks and, as expected, the maximum wind speed is still underestimated but there is a clear indication of a better agreement at the higher resolution. In particular, track intensities only exceed the Category 4 level under the future scenario in the 4 km simulations, a result which is shared with other two studies using 4 km resolution CPMs (Gutmann et al., 2018; Kanada et al., 2020). Present and future tracks for the 4 km simulations also seem to follow the same curve, that is, the increase in intensity is matched by a similar increase in depth in both simulations. Both models are in the range of resolutions capable of giving the correct range of depths (Chavas et al., 2017), showing storms exceeding the category 4 depths of the observed estimates (lower limit ~930 hPa, from Figure 10), and extending to category 5 depths in the future scenario (lower limit ~890 hPa). The result for the historical simulation is broadly consistent with the analysis from high resolution GCMs (~25 km resolution, Roberts et al., 2020) for the western Pacific, but it doesn't reach the wider range of the 6 km downscaled experiment of Knutson et al. (2015). The increased wind speed is clearly one of the factors leading to an improvement of this relationship in the 4 km CPM. However, mean sea level drop is also expected to depend on storm size (Chavas et al., 2017). The analysis of storm size, measured as the radius of maximum wind speed (not shown) indicates a larger distribution of radii from the 4 km model in the range between 10 and 150 km, while the 12 km RCM gives a range 25–100 km with a strong peak in the 25–50 km range. Observational estimates of outer radius for the North-West Pacific (e.g., Chavas et al., 2016 and reference therein) indicate this as the ocean basin with the most widely varying tropical storm size distribution, which might be more in agreement with the 4 km CPM result.

The effect of the increased resolution and changes under the greenhouse-gas forced scenarios on the intensity of tropical storms can be better assessed by a specific analysis on maximum wind speed over a common analysis region. Figure 11 shows Generalized Pareto Distributions (Coles, 2001) of maximum wind speed (a methodology already used in modeling tropical storm intensity, e.g., Jagger & Elsner, 2006), from tropical storms for all simulations, in comparison with tracks for the CMA data set included in IBTrACS (Knapp, Kruk, et al., 2010), for the period 1945–2016. The 80% uncertainty levels are estimated by profile likelihood (Coles, 2001): for the closely related Generalized Extreme Value analysis, non-overlapping uncertainty bands approximately correspond to a 10% significance level for the difference of the intensities from the two distributions (Kharin &
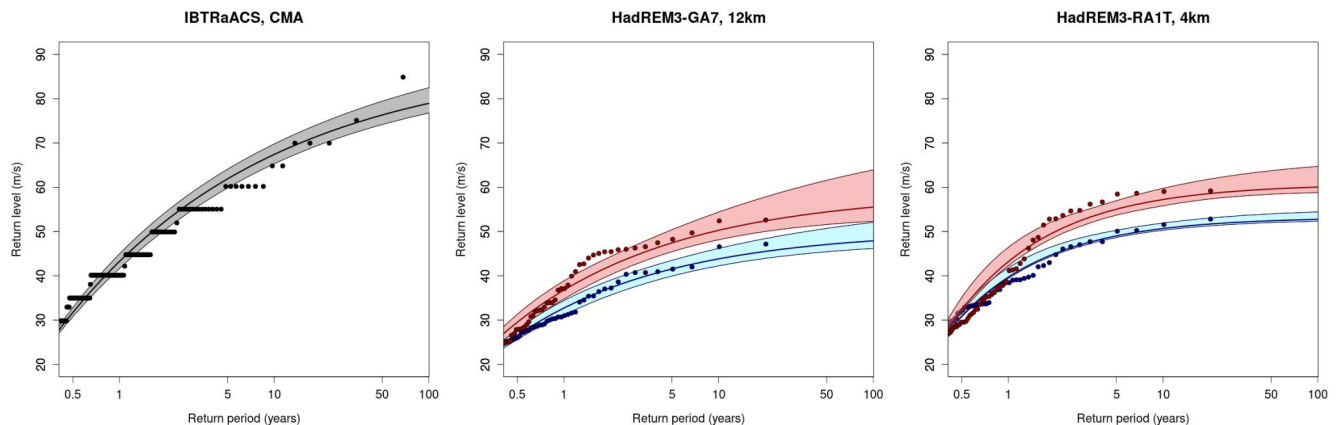
**Figure 11.** Return levels estimates from the Generalized Pareto Draistributions of maximum wind speed from tropical storm over the wider region of interest (Figure 1) for the Chinese Meteorological Administration tracks (1945–2016), left panel, for 12 km HadREM3-GA7 simulation, middle panel, and for the 4 km. HadREM3-RA1T simulations driven by the 12 km model, right panel (blue curves, all events from the historical period 1981–2000; red curves, all events from the RCP8.5 scenario, 2080–2099). For all plots, black dots represent the data sample, the middle curve is the GPD fit, the external curve represent the limits of the: 80% confidence interval estimated by the profile likelihood.

Zwiers, 2005). Since the set of tracks reaching the coastal region was not sufficient to generate converged uncertainty estimates for all the simulations, the set of tracks over the wider area of interest (117°–127°E, 26°–34°N, see Figure 1) have been used. This analysis clearly shows the larger range of maximum wind speed from 4 km CPM simulation with respect to that of maximum wind speed from their driving 12 km RCM simulations. The increase of intensity for longer return periods in both sets of simulations is rather strong and significant ($p < 0.1$), leading to a reduction of return periods by one order of magnitude for the upper end of the fitted curved for both runs. Average change in intensity from the 12 km simulations is 7.7% from an estimated mean of 27.1 m/s from the historical simulation, while the 4 km tropical storms give a slightly higher change 8.6% from a estimated mean of 32.2 m/s. Both changes are not significant ($p > 0.1$). In comparison with other projections for the wider basin (Knutson et al., 2020), after rescaling to 2°C global warming, these projections are in the range between the 25th-percentile and the median. It is also interesting to note that the estimates from observed and 12 km model tracks show heavier tails with respect to the 4 km model for both historical and future climate simulations, which seems to be in better agreement with the estimated curve from observed tracks. This could be related to the size of the domain: part of the spin up of the 4 km tracks seems to be happening on entering the 4 km domain, but there is also evidence of additional growth at least for the following 2 days, still likely to be associated with their sea portion of the tracks, raising the possibility that not all the detected 4 km tracks might have had the time to fully develop their higher resolution feature, even in a context of high variability as illustrated in Figure 9.

Figure 12 shows a composite analysis of the distribution of rainfall as a function of the grid box distance from the center of the storm at its peak intensity, composited from all tropical cyclone tracks in the two model nests and from observations (CMORPH, Joyce et al., 2004; Xie et al., 2019). As for the start of the analysis in this section, tracks have been selected by taking all the storms passing <100 km from the coastal region of eastern China and selecting their maximum intensity point within the region of interest (cf. Figure 1). In addition, tracks affected by the interaction with land have been discarded. Hourly precipitation has been calculated as the average of the preceding and the following hour, to have an estimate centered at the same time as the 3-hourly track; this procedure required a shift of the rainfall band position which takes into account the storm translational speed (i.e., rainfall bands were shifted along the great circle identified by the 3-hourly tracks). The same procedure has been applied to CMORPH data, with the additional complication of tropical cyclone centers coming from an independent source (CMA data set taken from IBTrACS), and not necessarily located in a place physically consistent with the rain band. As done in other similar analyses (e.g., Hence & Houze, 2011), these rain bands have been recentered over the CMA track location: as a result of this rather complex procedure, the resulting distribution does not show a neat drop at short distances like the distributions from the two models. The comparison of the observed rainfall distribution with the historical 4 km CPM rainfall distribution is reasonably good for peak intensity and position, while the 12 km RCM distribution has a very large wet bias at the peak; both models show a good representation of the distribution at larger distances. Also, it is worth noting that both models have a wider
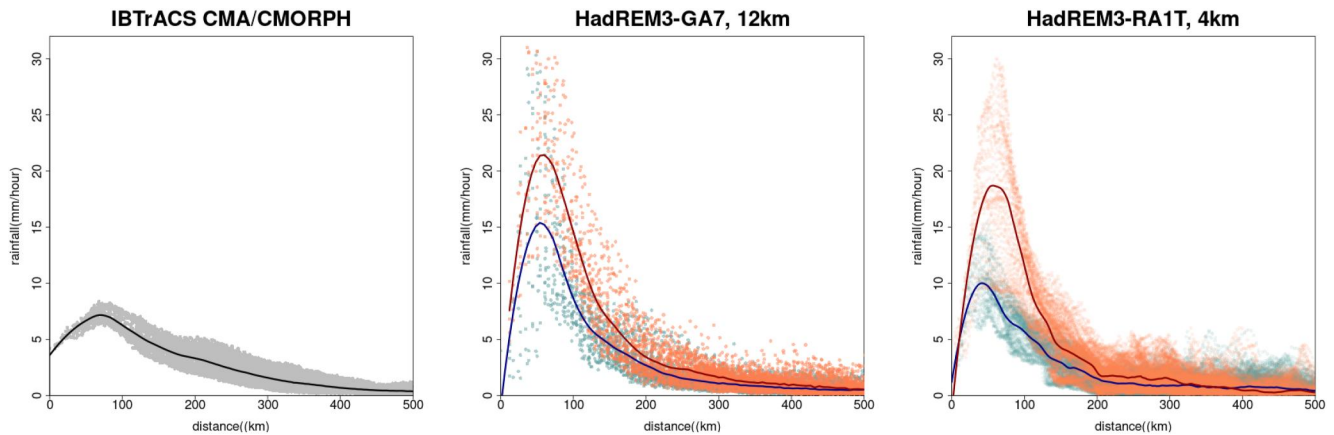
**Figure 12.** Rainfall (mm/hour) distribution from the center of storms from composites of tracks passing near the coast of eastern China. Left panel: distribution of rainfall for a tropical storm composite from CMORPH observations (1998–2016). Middle panel: HadREM3-GA7 12 km simulations: blue curve and points, historical period (1981–2000); red curve and points, rcp8.5 wind speed and rainfall distributions (2080–2099). Right panel: HadREM3-RA1T 12 km distributions, same order as above. Curves have been estimated by Local Polynomial Regression (loess, Cleveland et al., 1992, as implemented in the R software, R Core Team, 2019).

spread of data points mainly around the peak, not matched by the rather narrow distribution of the observation. Both model projections indicate a large increase in peak rainfall, 40% and 86% for the 12 km and the 4 km projections, respectively. Rainfall averaged over a 200 km radius estimates are 147 and 94 mm/day for the 12 and 4 km projections, respectively, while the estimate from observations is 117 mm/day which is also in better agreement with the result from the 4 km model. Changes for the 200 km average precipitation are 42% for the 12 km projection and 70% for the 4 km projection. These are two different changes: in comparison with the multi-model results from Knutson et al. (2020), after rescaling to 2°C global warming, the result from the 12 km model is below the 75th—percentile, while the 4 km model gives a change larger than all the other models. Both changes are also well above the Clausius-Clapeyron rate, approximately 7% increase per degree of local SST warming (Knutson et al., 2020), which is expected to determine the increase in atmospheric moisture over the ocean given the small projected change in relative humidity. An idealized climate change experiment (Liu et al., 2019) has indicated that changes in intensity could be the main factor explaining changes in rainfall rates exceeding the Clausius-Clapeyron rate, by showing that rainfall rates within each tropical storm category is basically consistent with the Clausius-Clapeyron limit, therefore mainly determined by the increased moisture available under climate change. For this analysis, the relatively small increase in intensity is also associated with a shift toward the higher end of the intensity distribution, which, according to the analysis of Liu et al. (2019), could be the main factor to explain the very high increase in rainfall rates.

The range of evaluation metrics used in this section indicates an improved description of tropical storms in the 4 km CPM model with respect to its driving 12 km model, with some indication of improved processes which would require more detailed analyses beyond the scope of this paper. The main climate change results, however, seem to have similar features in both model simulations, a result which should be taken as an additional indication of consistency between RCM and CPM.

## 5. Conclusions

A climate model experiment based on the use of a convection-permitting model at 4 km resolution has been used to generate climate projections of tropical cyclones in the region around Shanghai under greenhouse-gas forced scenarios. The experiment involves a double nesting set up with an outer 12 km and inner 4 km horizontal resolution limited areas driven by high-frequency 6-hourly atmospheric boundary conditions and daily SST and sea ice updates from the CMIP5 HadGEM2-ES simulations under the historical and RCP8.5 scenarios, for the periods 1981–2000 and 2080–2099 respectively. The change in global temperature from these projections is 4.8° C. The two Met Office state-of-the-art models used in the limited areas are the RCM HadREM3-GA7.05 (Tucker et al., 2022) at 12 km resolution and the convection-permitting model HadREM3-RA1T (based on Bush et al., 2019). The use of boundary conditions from a high-sensitivity GCM at the end of the 21st century under a very high greehouse-gas concentrations scenario is expected to produce one of the more extreme climate change

scenarios available from CMIP5 GCMs. As it is not unlikely to find significant bias in regional circulation from GCM historical simulations, the direct use of GCM boundary conditions needs a preliminary assessment of the model skill in reproducing the large-scale patterns relevant in a climate change study of tropical cyclones in the Shanghai area. This analysis has focused on large scale environmental variables relevant for formation and development of tropical storms, including SST, directly prescribed from the driving GCM in the double nesting experiment. Results show a very good agreement (bias <1°C) in the region of interest in summer and autumn (JJA and SON), the seasons of tropical storm activities, and on the representation of wind shear and its horizontal wind components in the same seasons. Biases related to the low-level circulation of the south Asian monsoon and to the weakening of the subtropical jet do not seem to affect the region of tropical storm development in the Shanghai area. In the future climate, the GCM projects a strong SST warming in the Shanghai region ($\sim$3.5°C) and a reduction of wind shear over a wider area of the West Pacific, with an associated increase of days favorable to the development of tropical storms. In summer, the reduction of wind shear is mostly associated to the weakening of the south Asian monsoon circulation, a robust result from GCM intercomparison projects, with a smaller impact from changes in upper-level jets in the West Pacific. The use of high frequency GCM atmospheric forcing keeps physical consistency of all these changes at a sub-daily time scale, a necessary requirement to capture the variability of weather systems. This would be rather difficult to reproduce from atmospheric perturbations at monthly or longer time scales as currently done in downscaled experiments based on the pseudo global warming approach, in particular for such a high range climate scenario projected by HadGEM2-ES under RCP8.5. The expected inclusion of the impact of robust circulation changes in the future climate scenario fully justified an approach which also relies on imperfect GCM forcing in the historical climate; in addition, potential links with available downscaling projections for CORDEX, in particular for the common setup used for the double nesting experiment, also support this approach.

These analyses also included an assessment of the consistency of the downscaled projections with the driving large scale conditions in the tropical storm seasons and with the climate change response of surface variables of the driving GCM. The results show good consistency in the circulation, in particular in the area of tropical storm development, and basic agreement with temperature and precipitation changes, in particular over the region of interest though there are some discrepancies in the 12 km RCM changes over the Pacific Ocean, potentially related to differences with the GCM driving circulation. Both downscaled models are wetter than the driving GCM over the analysis region, however, there is a clear improvement in the representation of the diurnal cycle of rainfall in the CPM projection, which is able to reproduce zonal changes and land sea differences in the timing of peak diurnal precipitation.

The analysis of the tropical cyclone statistics from the downscaled projections shows the expected refinement in representation of tropical storms in the 4 km CPM with respect to the 12 km RCM simulations. The two downscaled projections show similar frequency statistics in the present and future climate, but, despite the near perfect consistency of the 4 km CPM with its outer 12 km RCM nest at the scale of the latter, the correspondence of tropical storms is not perfectly biunivocal between the two models, that is, the percentage of 4 km CPM storms imported from the RCM are approximately 50%–60%, with the number of 4 km tracks systematically lower than those detected in the 12 km RCM simulations. In addition, this analysis shows a 11% increase in frequency of tropical storms over the area of interest around Shanghai from the 12 km simulations and a small decrease ($-2.5\%$) from the 4 km models, both not significant. The downscaled models project a change in seasonality, with the tropical storm season clearly extending to late autumn with respect to the historical period. The matching trajectories offer an opportunity to understand in more detail the effect of the increased resolution, showing an increase in intensity (measured as maximum wind speed) mainly realized before reaching the tracking area and therefore attributable to spin up processes at the edge of the CPM domain, and a slower increase over the rest of the lifetime of the storms. The 4 km CPM also shows a clear improvement in the relationship between minimum pressure and intensity with respect to the 12 km RCM, although both models underestimate the observed relationship of the most intense storms, with category 4–5 only reached by the 4 km CPM future climate simulation. However, in terms of relative frequency, both models project an increase in average tropical cyclone intensity for the end of century (2080-99) under RCP8.5, 7.7% and 8.6% respectively for the 12 km simulations and for the 4 km simulations, both not significant ($p > 0.1$). However, the extreme value analysis shows a significant reduction of return periods by one order of magnitude for the most extreme winds Finally, the representation of rainfall associated with tropical storms from both models shows a wet bias with respect to observation at short distances from the center of the storm, although maximum intensity is markedly improved in the 4 km CPM

simulation. There is also a good agreement at larger distances and for the average rainfall in a 200 km radius. Both downscaled models project a very strong increases of storm rainfall for the future climate exceeding 40% and 70% for the 12 and 4 km projections, respectively.

The 4 km CPM adds significant cost to these experiments and the main message of the projections is consistent between the two models. However, the 4 km model has a significantly improved pressure—intensity relationship, improves the representation of the rainbands and also better represents the diurnal cycle of precipitation These features which might be very important for example, when using downscaled projections for impact studies and suggests possible ways to improve the setup of future double nesting experiments.

Finally, these results do not assess some important sources of uncertainty. A single GCM has been used for projecting climate change from a single emissions scenario (RCP8.5). A more robust evaluation of future tropical cyclone risks for this region would be delivered by downscaling multiple GCMs for multiple RCPs. In addition this study used prescribed sea surface temperatures which have been shown to lead to positive biases in the tropical cyclone numbers and intensity, mainly due to not representing the cooling of SST caused by wind driven mixing in the ocean (Schade & Emanuel, 1999; Zarzycki et al., 2016). However, given the lack of high-resolution studies of tropical cyclone risk for this region, this study still offers valuable insights into the hazards facing the Shanghai region in the present and future from tropical cyclones. Results from these simulations have already been used in a flood modeling study by Ke et al. (2021) over Shanghai, in which changes in coastal flooding due to the combined effects of tropical cyclones, sea level rise and spring tide have been investigated.

## Data Availability Statement

The RCM HadREM3-GA7.05 and the convection permitting model HadREM3-RA1T are based on specific configuration of the Unified Model (UM, Brown et al., 2012) atmosphere and on the JULES (Best et al., 2011; Clarks et al., 2011) land. Due to intellectual property right restrictions, we cannot provide either the source code or documentation papers for the Met Office Unified Model (MetUM). The MetUM is available for use under license. For further information on how to apply for a license, see https://www.metoffice.gov.uk/research/approach/collaboration/unified-model/partnership. JULES is available under license free of charge. For further information on how to gain permission to use JULES for research purposes, see http://jules-lsm.github.io/access_req/JULES_access.html. Model output from all HadREM3-GA7.05 and HadREM3-RA1T simulations used in the paper are temporarily available at Dryad via [DOI] with Creative Common Zero 1.0 (Buonomo et al., 2024). Model HadGEM2-ES data from the historical and RCP8.5 simulations used as boundary conditions for the regional model experiment are available at the CMIP5 archive (https://pcmdi.llnl.gov/mips/cmip5/). For CMIP the U.S. Department of Energy's Program for Climate Model Diagnosis and Intercomparison provides coordinating support and led development of software infrastructure in partnership with the Global Organization for Earth System Science Portals. This data set also include the HadGEM2-ES data used in the analysis with the exception of daily horizontal winds at 850 hPa and 250 hPa from the historical simulation which have been included in the data distribution associated with this paper (Buonomo et al., 2024).

The NOAA OI SST v2 data set v2 (Huang et al., 2021; Reynolds et al., 2007) used for model evaluation is available at https://psl.noaa.gov/data/gridded/data.noaa.oisst.v2.highres.html. The ERA-Interim reanalysis data set (Berrisford et al., 2011) was provided by the European Centre for Medium-Range Weather Forecasts (ECMWF) at https://apps.ecmwf.int/data-catalogues/era-interim/?class=ei&stream=oper&expver=1. The observational near-surface temperature data used in this work are from CN05.1 (Wu & Gao, 2013), which is available at http://ccrc.iap.ac.cn/resource/detail?id=228. The Climate Prediction Center Morphing Method satellite-based rainfall estimates (Xie et al., 2019) were obtained from the publicly-available server at the Climate Prediction Center (CPC) of the National Oceanic and Atmospheric Administration (NOAA). Historical tracks from CMA were taken from IBTrACS (Knapp, Applequist, et al., 2010) v3.10 (Knapp, Applequist, et al., 2010), available at https://www.ncei.noaa.gov/access/metadata/landing-page/bin/iso?id=gov.noaa.ncdc:C00834.

## References

Amato, R., Steptoe, H., Buonomo, E., & Jones, R. (2019). High-resolution history: Downscaling China's climate from the 20CRv2c reanalysis. *Journal of Applied Meteorology and Climatology*, *58*(10), 2141–2157. https://doi.org/10.1175/JAMC-D-19-0083.1

Bates, D., Mächler, M., Bolker, B., & Walker, S. (2015). Fitting linear mixed-effects models using lme4. *Journal of Statistical Software*, *67*(1), 1–48. https://doi.org/10.18637/jss.v067.i01

Berrisford, P., Dee, D., Poli, P., Brugge, R., Fielding, M., Fuentes, M., et al. (2011). The ERA-Interim archive version 2.0 [Dataset]. ECMWF. Retrieved from https://apps.ecmwf.int/data-catalogues/era-interim/?class=ei&stream=oper&expver=1

Best, M. J., Pryor, M., Clark, D. B., Rooney, G. G., Essery, R. L. H., Ménard, C. B., et al. (2011). The Joint UK Land Environment Simulator (JULES), model description – Part 1: Energy and water fluxes. *Geoscientific Model Development*, *4*(3), 677–699. https://doi.org/10.5194/gmd-4-677-2011

Brown, A., Milton, S., Cullen, M., Golding, B., Mitchell, J., & Shelly, A. (2012). Unified modeling and prediction of weather and climate: A 25-year journey. *Bulletin of the American Meteorological Society*, *93*(12), 1865–1877. https://doi.org/10.1175/BAMS-D-12-00018.1

Buonomo, E., Savage, N., Redmond, G., & Tucker, S. (2024). Climate model output from a study of tropical cyclones over the Shanghai region under climate change based on a convection-permitting modelling [Dataset]. Dryad. https://doi.org/10.5061/dryad.z8w9ghxgq

Bush, M., Allen, T., Bain, C., Boutle, I., Edwards, J., Finnenkoetter, A., et al. (2019). The first Met Office unified model/JULES regional atmosphere and land configuration, RAL1. *Geoscientific Model Development*, *13*, 1999–2029. https://doi.org/10.5194/gmd-13-1999-2020

Camargo, S. J. (2013). Global and regional aspects of tropical cyclone activity in the CMIP5 models. *Journal of Climate*, *26*(24), 9880–9902. https://doi.org/10.1175/JCLI-D-12-00549.1

Camp, J., Roberts, M. J., Comer, R. E., Wu, P. L., MacLachlan, C., Bett, P. E., et al. (2019). The western Pacific subtropical high and tropical cyclone landfall: Seasonal forecasts using the Met Office GloSea5 system. *Quarterly Journal of the Royal Meteorological Society*, *145*(718), 105–116. https://doi.org/10.1002/qj.3407

Cécé, R., Bernard, D., Krien, Y., Leone, F., Candela, T., Péroche, M., et al. (2021). A 30 m scale modeling of extreme gusts during Hurricane Irma (2017) landfall on very small mountainous islands in the Lesser Antilles. *Natural Hazards and Earth System Sciences*, *21*(1), 129–145. https://doi.org/10.5194/nhess-21-129-2021

Chavas, D. R., Lin, N., Dong, W., & Lin, Y. (2016). Observed tropical cyclone size revisited. *Journal of Climate*, *29*(8), 2923–2939. https://doi.org/10.1175/JCLI-D-15-0731.1

Chavas, D. R., Reed, K. A., & Knaff, J. A. (2017). Physical understanding of the tropical cyclone wind-pressure relationship. *Nature Communications*, *8*(1), 1360. https://doi.org/10.1038/s41467-017-01546-9

Chen, T., Chen, S., Zhou, M., Tu, C., Zhang, A., Chen, Y., & Li, W. (2022). Northward shift in landfall locations of tropical cyclones over the Western North Pacific during the last four decades. *Advances in Atmospheric Sciences*, *39*(2), 304–319. https://doi.org/10.1007/s00376-021-1077-z

Clark, D. B., Mercado, L. M., Sitch, S., Jones, C. D., Gedney, N., Best, M. J., et al. (2011). The Joint UK Land Environment Simulator (JULES), model description – Part 2: Carbon fluxes and vegetation dynamics. *Geoscientific Model Development*, *4*(3), 701–722. https://doi.org/10.5194/gmd-4-701-2011

Cleveland, W. S., Grosse, E., & Shyu, W. M. (1992). Local regression models. In J. M. Chambers & T. J. Hastie (Eds.), *Statistical models in S* (pp. 309–376). Wadsworth & Brooks/Cole.

Coles, S. (2001). *An introduction to statistical modeling of extreme values*. Springer Verlag.

Collins, W. J., Bellouin, N., Doutriaux-Boucher, M., Gedney, N., Halloran, P., Hinton, T., et al. (2011). Development and evaluation of an earth-system model – HadGEM2. *Geoscientific Model Development*, *4*(4), 1051–1075. https://doi.org/10.5194/gmd-4-1051-2011

Davies, T. (2014). Lateral boundary conditions for limited area models. *Quarterly Journal of the Royal Meteorological Society*, *140*(678), 185–196. https://doi.org/10.1002/qj.2127

Dee, D. P., Uppala, S. M., Simmons, A. J., Berrisford, P., Poli, P., Kobayashi, S., et al. (2011). The ERA-interim reanalysis: Configuration and performance of the data assimilation system. *Quarterly Journal of the Royal Meteorological Society*, *137*(656), 553–597. https://doi.org/10.1002/qj.828

Done, J. M., Lackmann, G. M., & Prein, A. F. (2022). The response of tropical cyclone intensity to changes in environmental temperature. *Weather and Climate Dynamics*, *3*(2), 693–711. https://doi.org/10.5194/wcd-3-693-2022

Emanuel, K. A., & Nolan, D. S. (2004). Tropical cyclone activity and global climate system. In *Proceedings of 26th conference on hurricanes and tropical meteorology* (pp. 240–241). American Meteorological Society.

Emanuel, K. A. (1987). The dependence of hurricane intensity on climate. *Nature*, *326*(6112), 483–485. https://doi.org/10.1038/326483a0

Fengjin, X., & Ziniu, X. (2010). Characteristics of tropical cyclones in China and their impacts analysis. *Natural Hazards*, *54*(3), 827–837. https://doi.org/10.1007/s11069-010-9508-7

Fiedler, S., Stevens, B., Gidden, M., Smith, S. J., Riahi, K., & van Vuuren, D. (2019). First forcing estimates from the future CMIP6 scenarios of anthropogenic aerosol optical properties and an associated Twomey effect. *Geoscientific Model Development*, *12*(3), 989–1007. https://doi.org/10.5194/gmd-12-989-2019

Fosser, G., Kendon, E., Chan, S., Lock, A., Roberts, N., & Bush, M. (2020). Optimal configuration and resolution for the first convection-permitting ensemble of climate projections over the United Kingdom. *International Journal of Climatolology*, *40*(7), 3585–3606. https://doi.org/10.1002/joc.6415

Gallo, F., Daron, J., Macadam, I., Cinco, T., Villafuerte, M., II, Buonomo, E., et al. (2019). High-resolution regional climate model projections of future tropical cyclone activity in the Philippines. *International Journal of Climatology*, *39*(3), 1181–1194. https://doi.org/10.1002/joc.5870

Gentry, M. S., & Lackmann, G. M. (2010). Sensitivity of simulated tropical cyclone structure and intensity to horizontal resolution. *Monthly Weather Review*, *138*(3), 688–704. https://doi.org/10.1175/2009MWR2976.1

Gettelman, A., Bresch, D. N., Chen, C. C., Truesdale, J. E., & Basmeister, J. T. (2018). Projections of future tropical cyclone damage with a high-resolution global climate model. *Climatic Change*, *146*(3–4), 575–585. https://doi.org/10.1007/s10584-017-1902-7

Giorgi, F., Jones, C., & Asrar, G. (2009). Addressing climate information needs at the regional level: The CORDEX framework. *World Meteorological Organization Bulletin*, *58*(3), 175.

Gray, W. M. (1998). The formation of tropical cyclones. *Meteorology and Atmospheric Physics*, *67*(1–4), 37–69. https://doi.org/10.1007/BF01277501

Gregory, D., & Rowntree, P. R. (1990). A mass flux convection scheme with representation of cloud ensemble characteristics and stability-dependent closure. *Monthly Weather Review*, *118*(7), 1483–1506. https://doi.org/10.1175/1520-0493(1990)118<1483:AMFCSW>2.0.CO;2

Gutmann, E. D., Rasmussen, R. M., Liu, C., Ikeda, K., Bruyere, C. L., Done, J. M., et al. (2018). Changes in hurricanes from a 13-yr convection-permitting pseudo–global warming simulation. *Journal of Climate*, *31*(9), 3643–3657. https://doi.org/10.1175/JCLI-D-17-0391.1

Hanson, B., Klink, K., Matsuura, K., Robeson, S. M., & Willmott, C. J. (1992). Vector correlation: Review, exposition, and geographic application. *Annals of the Association of American Geographers*, *82*(1), 103–116. https://doi.org/10.1111/j.1467-8306.1992.tb01900.x

Hence, D. A., & Houze, R. A. (2011). Vertical structure of hurricane eyewalls as seen by the TRMM precipitation radar. *Journal of the Atmospheric Sciences*, *68*(8), 1637–1652. https://doi.org/10.1175/2011JAS3578.1

Holland, G. J., Belanger, J. I., & Fritz, A. (2010). A revised model for radial profiles of hurricane winds. *Monthly Weather Review*, *138*(12), 4393–4401. https://doi.org/10.1175/2010MWR3317.1

Huang, B., Liu, C., Banzon, V., Freeman, E., Graham, G., Hankins, B., et al. (2021). Improvements of the daily optimum interpolation sea surface temperature (DOISST) version 2.1. *Journal of Climate*, *34*(8), 2923–2939. https://doi.org/10.1175/JCLI-D-20-0166.1

Huang, S., Wang, B., & Wen, Z. (2020). Dramatic weakening of the tropical easterly jet projected by CMIP6 models. *Journal of Climate*, *33*(19), 8439–8455. https://doi.org/10.1175/JCLI-D-19-1002.1

Hurtt, G. C., Chini, L. P., Frolking, S., Betts, R. A., Fischer, G., Fisk, J. P., et al. (2011). Harmonization of land-use scenarios for the period 1500–2100: 600 years of global gridded annual land-use transitions, wood harvest, and resulting secondary lands. *Climatic Change*, *109*(1–2), 117–161. https://doi.org/10.1007/s10584-011-0153-2

Jagger, T. H., & Elsner, J. B. (2006). Climatology models for extreme hurricane winds near the United States. *Journal of Climate*, *19*(13), 3220–3236. https://doi.org/10.1175/JCLI3913.1

Jiang, Z., Tian, Z., Dong, G., Sun, L., Zhang, P., Buonomo, E., & Fan, D. (2020). High-resolution projections of mean and extreme precipitation over China by two regional climate models. *Journal of Meteorological Research*, *34*(5), 965–985. https://doi.org/10.1007/s13351-020-9208-5

Jones, C. D., Hughes, J. K., Bellouin, N., Hardiman, S. C., Jones, G. S., Knight, J., et al. (2011). The HadGEM2-ES implementation of CMIP5 centennial simulations. *Geoscientific Model Development*, *4*(3), 543–570. https://doi.org/10.5194/gmd-4-543-2011

Jones, R. G., Murphy, J. M., & Noguer, M. (1995). Simulation of climate change over Europe using a nested regional-climate model. I: Assessment of control climate, including sensitivity to location of lateral boundaries. *Quarterly Journal of the Royal Meteorological Society*, *121*(526), 1413–1449. https://doi.org/10.1002/qj.49712152610

Joyce, R. J., Janowiak, J. E., Arkin, P. A., & Xie, P. P. (2004). CMORPH: A method that produces global precipitation estimates from passive microwave and infrared data at high spatial and temporal resolution. *Journal of Hydrometeorology*, *5*(3), 487–503. https://doi.org/10.1175/1525-7541(2004)005<0487:Camtpg>2.0.CO;2

Kanada, S., Takemi, T., Kato, M., Yamasaki, S., Fudeyasu, H., Tsuboki, K., et al. (2017). A multimodel intercomparison of an intense typhoon in future, warmer climates by four 5-km-Mesh models. *Journal of Climate*, *30*(15), 6017–6036. https://doi.org/10.1175/JCLI-D-16-0715.1

Kanada, S., Tsuboki, K., & Takayabu, I. (2020). Future changes of tropical cyclones in the midlatitudes in 4-km-mesh downscaling experiments from large-ensemble simulations. *Scientific Online Letters on the Atmosphere*, *16*(0), 57–63. https://doi.org/10.2151/sola.2020-010

Kanada, S., Wada, A., & Sugi, M. (2013). Future changes in structures of extremely intense tropical cyclones using a 2-km mesh nonhydrostatic model. *Journal of Climate*, *26*(24), 9986–10005. https://doi.org/10.1175/JCLI-D-12-00477.1

Ke, Q., Yin, J., Bricker, J. D., Savage, N., Buonomo, E., Ye, Q., et al. (2021). An integrated framework of coastal flood modelling under the failures of sea dikes: A case study in Shanghai. *Natural Hazards*, *109*(1), 671–703. https://doi.org/10.1007/s11069-021-04853-z

Kharin, V. V., & Zwiers, F. W. (2005). Estimating extremes in transient climate change simulations. *Journal of Climate*, *18*(8), 1156–1173. https://doi.org/10.1175/JCLI3320.1

Knapp, K. R., Applequist, S., Diamond, H. J., Kossin, J. P., Kruk, M., & Schreck, C. (2010). *NCDC International Best Track Archive for Climate Stewardship (IBTrACS) project, version 3.10*. NOAA National Centers for Environmental Information. https://doi.org/10.7289/V5NK3BZP

Knapp, K. R., Kruk, M. C., Levinson, D. H., Diamond, H. J., & Neumann, C. J. (2010). The international best track archive for climate stewardship (IBTrACS). *Bulletin of the American Meteorological Society*, *91*(3), 363–376. https://doi.org/10.1175/2009BAMS2755.1

Knutson, T., Camargo, S. J., Chan, J. C. L., Emanuel, K., Ho, C., Kossin, J., et al. (2020). Tropical cyclones and climate change assessment: Part II: Projected response to anthropogenic warming. *Bulletin of the American Meteorological Society*, *101*(3), E303–E322. https://doi.org/10.1175/BAMS-D-18-0194.1

Knutson, T., Sirutis, J. J., Bender, M. A., Tuleya, R. E., & Schenkel, B. A. (2022). Dynamical downscaling projections of late twenty-first-century US landfalling hurricane activity. *Climatic Change*, *171*(3–4), 28. https://doi.org/10.1007/s10584-022-03346-7

Knutson, T. R., Sirutis, J. J., Vecchi, G. A., Garner, S., Zhao, M., Kim, H., et al. (2013). Dynamical downscaling projections of twenty-first-century Atlantic hurricane activity: CMIP3 and CMIP5 model-based scenarios. *Journal of Climate*, *26*(17), 6591–6617. https://doi.org/10.1175/JCLI-D-12-00539.1

Knutson, T. R., Sirutis, J. J., Zhao, M., Tuleya, R. E., Bender, M., Vecchi, G. A., et al. (2015). Global projections of intense tropical cyclone activity for the late twenty-first century from dynamical downscaling of CMIP5/RCP4.5 scenarios. *Journal of Climate*, *28*(18), 7203–7224. https://doi.org/10.1175/jcli-d-15-0129.1

Knutson, T. R., & Tuleya, R. E. (2004). Impact of CO2-induced warming on simulated hurricane intensity and precipitation: Sensitivity to the choice of climate model and convective parameterization. *Journal of Climate*, *17*(18), 3477–3495. https://doi.org/10.1175/1520-0442(2004)017<3477:IOCWOS>2.0.CO;2

Kossin, J., Emanuel, K., & Vecchi, G. (2014). The poleward migration of the location of tropical cyclone maximum intensity. *Nature*, *509*(7500), 349–352. https://doi.org/10.1038/nature13278

Kossin, J. P. (2018). A global slowdown of tropical-cyclone translation speed. *Nature*, *558*(7708), 104–107. https://doi.org/10.1038/s41586-018-0158-3

Kossin, J. P., Emanuel, K. A., & Camargo, S. J. (2016). Past and projected changes in Western North Pacific tropical cyclone exposure. *Journal of Climate*, *29*(16), 5725–5739. https://doi.org/10.1175/JCLI-D-16-0076.1

Leduc, M., & Laprise, R. (2009). Regional climate model sensitivity to domain size. *Climate Dynamics*, *32*(6), 833–854. https://doi.org/10.1007/s00382-008-0400-z

Liu, M., Vecchi, G. A., Smith, J. A., & Knutson, T. R. (2019). Causes of large projected increases in hurricane precipitation rates with global warming. *NPJ Climate and Atmospheric Science*, *2*(1), 38. https://doi.org/10.1038/s41612-019-0095-3

Lorenz, E. N. (1969). Atmospheric predictability as revealed by naturally occurring analogues. *Journal of the Atmospheric Sciences*, *26*(4), 636–646. https://doi.org/10.1175/1520-0469(1969)26<636:APARBN>2.0.CO;2

Magee, A. D., Verdon-Kidd, D. C., & Kiem, A. S. (2016). An intercomparison of tropical cyclone best-track products for the southwest Pacific. *Natural. Hazards and Earth System Science*, *16*(6), 1431–1447. https://doi.org/10.5194/nhess-16-1431-2016

McSweeney, C. F., Jones, R. G., Lee, R. W., & Rowell, D. P. (2015). Selecting CMIP5 GCMs for downscaling over multiple regions. *Climate Dynamics*, *44*(11–12), 3237–3260. https://doi.org/10.1007/s00382-014-2418-8

Mendelsohn, R., Emanuel, K., Chonabayashi, S., & Bakkensen, L. (2012). The impact of climate change on global tropical cyclone damage. *Nature Climate Change*, *2*(3), 205–209. https://doi.org/10.1038/nclimate1357

Miller, B. I. (1958). On the maximum intensity of hurricanes. *Journal of the Atmospheric Sciences*, *15*(2), 184–195. https://doi.org/10.1175/1520-0469(1958)015⟨0184:OTMIOH⟩2.0.CO;2

Mittal, R., Tewari, M., Radhakrishnan, C., Ray, P., Singh, T., & Nickerson, A. K. (2019). Response of tropical cyclone Phailin (2013) in the Bay of Bengal to climate perturbations. *Climate Dynamics*, *53*(3–4), 2013–2030. https://doi.org/10.1007/s00382-019-04761-w

Mizuta, R., Murata, A., Ishii, M., Shiogama, H., Hibino, K., Mori, N., et al. (2017). Over 5,000 years of ensemble future climate simulations by 60-km global and 20-km regional atmospheric models. *Bulletin of the American Meteorological Society*, *98*(7), 1383–1398. https://doi.org/10.1175/BAMS-D-16-0099.1

Moufouma-Okia, W., & Jones, R. (2015). Resolution dependence in simulating the African hydroclimate with the HadGEM3-RA regional climate model. *Climate Dynamics*, *44*(3–4), 609–632. https://doi.org/10.1007/s00382-014-2322-2

Murphy, J. M., Harris, G. R., Sexton, D. M. H., Kendon, E. J., Bett, R. T., Clark, K. E., et al. (2019). UKCP18 land projections: Science report. Retrieved from https://www.metoffice.gov.uk/pub/data/weather/uk/ukcp18/science-reports/UKCP18-Land-report.pdf

Nikulin, G., Jones, C., Giorgi, F., Asrar, G., Büchner, M., Cerezo-Mota, R., et al. (2012). Precipitation climatology in an ensemble of CORDEX-Africa regional climate simulations. *Journal of Climate*, *25*(18), 6057–6078. https://doi.org/10.1175/JCLI-D-11-00375.1

Pinheiro, J., Bates, D., DebRoy, S., & Sarkar, D., & R Core Team. (2021). NLME: Linear and nonlinear mixed effects models. R package version 3.1-152. Retrieved from https://CRAN.R-project.org/package=nlme

Pinheiro, J., & Bates, D. M. (2000). *Mixed effects models in S and S -PLUS*. Springer-Verlag.

Prein, A. F., Langhans, W., Fosser, G., Ferrone, A., Ban, N., Goergen, K., et al. (2015). A review on regional convection-permitting climate modeling: Demonstrations, prospects, and challenges. *Reviews of Geophysics*, *53*(2), 323–361. https://doi.org/10.1002/2014RG000475

R Core Team. (2019). *R: A language and environment for statistical computing*. R Foundation for Statistical Computing. Retrieved from https://www.R-project.org

Reynolds, R. W., Smith, T. M., Liu, C., Chelton, D. B., Casey, K. S., & Schlax, M. G. (2007). Daily high-resolution-blended analyses for Sea Surface temperature. *Journal of Climate*, *20*(22), 5473–5496. https://doi.org/10.1175/2007JCLI1824.1

Roberts, M. J., Camp, J., Seddon, J., Vidale, P. L., Hodges, K., Vanniere, B., et al. (2020). Impact of model resolution on tropical cyclone simulation using the HighResMIP–PRIMAVERA multimodel ensemble. *Journal of Climate*, *33*(7), 2557–2583. https://doi.org/10.1175/JCLI-D-19-0639.1

Rotunno, R., Chen, Y., Wang, W., Davis, C., Dudhia, J., & Holland, G. J. (2009). Large-eddy simulation of an idealized tropical cyclone. *Bulletin of the American Meteorological Society*, *90*(12), 1783–1788. https://doi.org/10.1175/2009BAMS2884.1

Sanchez-Gomez, E., Somot, S., & Déqué, M. (2009). Ability of an ensemble of regional climate models to reproduce weather regimes over Europe-Atlantic during the period 1961–2000. *Climate Dynamics*, *33*(5), 723–736. https://doi.org/10.1007/s00382-008-0502-7

Schade, L. R., & Emanuel, K. A. (1999). The Ocean's effect on the intensity of tropical cyclones: Results from a simple coupled atmosphere–ocean model. *Journal of the Atmospheric Sciences*, *56*(4), 642–651. https://doi.org/10.1175/1520-0469(1999)056<0642:TOSEOT>2.0.CO;2

Schär, C., Frei, C., Lüthi, D., & Davies, H. C. (1996). Surrogate climate-change scenarios for regional climate models. *Geophysisical. Research Letters*, *23*(6), 669–672. https://doi.org/10.1029/96GL00265

Smith, R. N. B. (1990). A scheme for predicting layer cloud and their water content in a general circulation model. *Quarterly Journal of the Royal Meteorological Society*, *116*(492), 435–460. https://doi.org/10.1002/qj.49711649210

Sobel, A. H., Wing, A. A., Camargo, S. J., Patricola, C. M., Vecchi, G. A., Lee, C.-Y., & Tippett, M. K. (2021). Tropical cyclone frequency. *Earth's Future*, *9*(12), e2021EF002275. https://doi.org/10.1029/2021EF002275

Stevens, B., Fiedler, S., Kinne, S., Peters, K., Rast, S., Müsse, J., et al. (2017). MACv2-SP: A parameterization of anthropogenic aerosol optical properties and an associated Twomey effect for use in CMIP6. *Geoscientific Model Development*, *10*(1), 433–452. https://doi.org/10.5194/gmd-10-433-2017

Sugi, M., Yoshida, K., & Murakami, H. (2015). More tropical cyclones in a cooler climate? *Geophysical Research Letters*, *42*(16), 6780–6784. https://doi.org/10.1002/2015GL064929

Taraphdar, S., Mukhopadhyay, P., Leung, L. R., Zhang, F., Abhilash, S., & Goswami, B. N. (2014). The role of moist processes in the intrinsic predictability of Indian Ocean cyclones. *Journal of Geophysical Research: Atmospheres*, *119*(13), 8032–8048. https://doi.org/10.1002/2013JD021265

Taylor, K. E., Stouffer, R. J., & Meehl, G. A. (2012). An overview of CMIP5 and the experiment design. *Bulletin of the American Meteorological Society*, *93*(4), 485–498. https://doi.org/10.1175/BAMS-D-11-00094.1

Thompson, C., Barthe, C., Bielli, S., Tulet, P., & Pianezze, J. (2021). Projected characteristic changes of a typical tropical cyclone under climate change in the South West Indian Ocean. *Atmosphere*, *12*(2), 232. https://doi.org/10.3390/atmos12020232

Tory, K. J., Chand, S. S., McBride, J. L., Ye, H., & Dare, R. A. (2013). Projected changes in late-twenty-first-century tropical cyclone frequency in 13 coupled climate models from phase 5 of the coupled model intercomparison project. *Journal of Climate*, *26*(24), 9946–9959. https://doi.org/10.1175/JCLI-D-13-00010.1

Tsou, C. H., Pei-Yu, H., Tu, C. Y., Cheng-Ta, C., Tzeng, T. P., & Cheng, C. T. (2016). Present simulation and future typhoon activity projection over western North Pacific and Taiwan/East Coast of China in 20-km HiRAM climate model. *TAO: Terrestrial, Atmospheric and Oceanic Sciences*, *27*(5), 6. https://doi.org/10.3319/TAO.2016.06.13.04

Tucker, S. O., Kendon, E. J., Bellouin, N., Buonomo, E., Johnson, B., & Murphy, J. M. (2022). Evaluation of a new 12 km regional perturbed parameter ensemble over Europe. *Climate Dynamics*, *58*(3–4), 879–903. https://doi.org/10.1007/s00382-021-05941-3

Tuleya, R. E., Bender, M., Knutson, T. R., Sirutis, J. J., Thomas, B., & Ginis, I. (2016). Impact of upper-tropospheric temperature anomalies and vertical wind shear on tropical cyclone evolution using an idealized version of the operational GFDL hurricane model. *Journal of the Atmospheric Sciences*, *73*(10), 3803–3820. https://doi.org/10.1175/JAS-D-16-0045.1

Ullrich, P. A., & Zarzycki, C. M. (2017). TempestExtremes: A framework for scale-insensitive pointwise feature tracking on unstructured grids. *Geoscientific Model Development*, *10*(3), 1069–1090. https://doi.org/10.5194/gmd-10-1069-2017

van Vuuren, D. P., Edmonds, J., Kainuma, M., Riahi, K., Thomson, A., Hibbard, K., et al. (2011). The representative concentration pathways: An overview. *Climatic Change*, *109*(1–2), 5–31. https://doi.org/10.1007/s10584-011-0148-z

Walters, D., Baran, A. J., Boutle, I., Brooks, M., Earnshaw, P., Edwards, J., et al. (2019). The Met Office unified model global atmosphere 7.0/7.1 and JULES global land 7.0 configurations. *Geoscientific Model Development*, *12*(5), 1909–1963. https://doi.org/10.5194/gmd-12-1909-2019

Wang, B., Biasutti, M., Byrne, M. P., Castro, C., Chang, C., Cook, K., et al. (2021). Monsoons climate change assessment. *Bulletin of the American Meteorological Society*, *102*(1), E1–E19. https://doi.org/10.1175/BAMS-D-19-0335.1

Wang, Y., Wen, S., Li, X., Thomas, F., Su, B., Wang, R., & Jiang, T. (2016). Spatiotemporal distributions of influential tropical cyclones and associated economic losses in China in 1984–2015. *Natural Hazards*, *84*(3), 2009–2030. https://doi.org/10.1007/s11069-016-2531-6

Wilcoxon, F. (1945). Individual comparisons by ranking methods. *Biometrics Bulletin*, *1*(6), 80–83. https://doi.org/10.2307/3001968

Wilson, D. R., & Ballard, S. P. (1999). A microphysically based precipitation scheme for the UK meteorological office unified model. *Quarterly Journal of the Royal Meteorological Society*, *125*(557), 1607–1636. https://doi.org/10.1002/qj.49712555707

Wu, J., & Gao, X. J. (2013). A gridded daily observation dataset over China region and comparison with the other datasets. *Chinese Journal of Geophysics*, *56*, 1102–1111. https://doi.org/10.6038/cjg20130406

Wu, L., Chou, C., Chen, C., Huang, R., Knutson, T. R., Sirutis, J. J., et al. (2014). Simulations of the present and late-twenty-first-century Western North Pacific tropical cyclone activity using a regional model. *Journal of Climate*, *27*(9), 3405–3424. https://doi.org/10.1175/JCLI-D-12-00830.1

Wu, L., Wang, B., & Geng, S. (2005). Growing typhoon influence on East Asia. *Geophysical Research Letters*, *32*(18), L18703. https://doi.org/10.1029/2005GL022937

Xie, P., Joyce, R., Wu, S., Yoo, S.-H., Yarosh, Y., Sun, F., & Lin, R. (2019). NOAA climate data record (CDR) of CPC morphing technique (CMORPH) high resolution global precipitation estimates, version 1a [Dataset]. NOAA National Centers for Environmental Information. https://doi.org/10.25921/w9va-q159

Xu, J., & Wang, Y. (2018). Dependence of tropical cyclone intensification rate on sea surface temperature, storm intensity, and size in the western North Pacific. *Weather and Forecasting*, *33*(2), 523–537. https://doi.org/10.1175/WAF-D-17-0095.1

Zarzycki, C. M. (2016). Tropical cyclone intensity errors associated with lack of two-way ocean coupling in high-resolution global simulations. *Journal of Climate*, *29*(23), 8589–8610. https://doi.org/10.1175/JCLI-D-16-0273.1

Zhang, F., Snyder, C., & Rotunno, R. (2003). Effects of moist convection on mesoscale predictability. *Journal of the Atmospheric Sciences*, *60*(9), 1173–1185. https://doi.org/10.1175/1520-0469(2003)060<1173:EOMCOM>2.0.CO;2